ADVANCING EARTH AND SPACE SCIENCES

Water Resources Research®

RESEARCH ARTICLE
10.1029/2024WR037834

Quantification of Carbopeaking and CO_2 Fluxes in a Regulated Alpine River

G. Dolcetti[1], S. Piccolroaz[1], M. C. Bruno[2,3], E. Calamita[4], S. Larsen[2,3], G. Zolezzi[1], and A. Siviglia[1]

[1]Department of Civil, Environmental and Mechanical Engineering, University of Trento, Trento, Italy, [2]Research and Innovation Centre, Fondazione Edmund Mach, San Michele all'Adige, Italy, [3]NBFC, National Biodiversity Future Center, Palermo, Italy, [4]Department Surface Waters - Research and Management, Eawag, Dübendorf, Switzerland

Key Points:

- Flow regulation in an Alpine river affects the spatiotemporal variability and drivers of CO_2 fluxes
- Diel metabolism and carbonate buffering sustained by lateral inflows dominate CO_2 dynamics in the residual flow reaches
- Intense and localized peaks in CO_2 concentration and evasion rate are observed downstream of the hydropower outlets during hydropeaking

Supporting Information:

Supporting Information may be found in the online version of this article.

Correspondence to:

G. Dolcetti,
giulio.dolcetti@unitn.it

Citation:

Dolcetti, G., Piccolroaz, S., Bruno, M. C., Calamita, E., Larsen, S., Zolezzi, G., & Siviglia, A. (2025). Quantification of carbopeaking and CO_2 fluxes in a regulated Alpine river. *Water Resources Research*, *61*, e2024WR037834. https://doi.org/10.1029/2024WR037834

Received 24 APR 2024
Accepted 13 JAN 2025

Author Contributions:

Conceptualization: G. Dolcetti, S. Larsen, A. Siviglia
Data curation: G. Dolcetti
Formal analysis: G. Dolcetti, A. Siviglia
Funding acquisition: G. Zolezzi, A. Siviglia
Investigation: S. Piccolroaz, M. C. Bruno, E. Calamita, S. Larsen, A. Siviglia
Methodology: G. Dolcetti, S. Piccolroaz, A. Siviglia
Software: G. Dolcetti
Visualization: G. Dolcetti
Writing – original draft: G. Dolcetti
Writing – review & editing: G. Dolcetti, S. Piccolroaz, M. C. Bruno, E. Calamita, S. Larsen, G. Zolezzi, A. Siviglia

Abstract Carbon dioxide (CO_2) fluxes in regulated Alpine rivers are driven by multiple biogeochemical and anthropogenic processes, acting on different spatiotemporal scales. We quantified the relative importance of these drivers and their effects on the dynamics of CO_2 concentration and atmospheric exchange fluxes in a representative Alpine river segment regulated by a cascading hydropower system with diversion, which includes two residual flow reaches and a reach subject to hydropeaking. We combined instantaneous and time-resolved water chemistry and hydraulic measurements at different times of the year, and quantified the main CO_2 fluxes by calibrating a one-dimensional transport-reaction model with measured data. As a novelty compared to previous inverse modeling applications, the model also included carbonate buffering, which contributed significantly to the CO_2 budget of the case study. The spatiotemporal distribution and drivers of CO_2 fluxes depended on hydropower operations. Along the residual flow reaches, CO_2 fluxes were directly affected by the upstream dams only in the first ∼2.5 km, where the supply of supersaturated water from the reservoirs was predominant. Downstream of the hydropower diversion outlets, the CO_2 fluxes were dominated by systematic sub-daily fluctuations in CO_2 transport and evasion fluxes ("carbopeaking") driven by hydropeaking. Hydropower operational patterns and regulation approaches in Alpine rivers affect CO_2 fluxes and their response to biogeochemical drivers significantly across different temporal scales. Our findings highlight the importance of considering all scales of CO_2 variations for accurate quantification and understanding of these impacts, to clarify the role of natural and anthropogenic drivers in global carbon cycling.

Plain Language Summary Rivers play a key role in the transport, processing and exchange of carbon and CO_2 between land, atmosphere, and oceans. CO_2 fluxes are governed by biological, chemical, and hydraulic processes which may be perturbed by human activities, such as hydropower. Understanding and quantifying these effects is challenging due to the various processes and temporal and spatial scales involved. We conducted an extensive measurement campaign over several days and across all seasons along an Alpine river where hydropower strongly affects hydraulic conditions, and used the data to calibrate a numerical model and estimate the main sources of CO_2 fluxes. CO_2 levels were high near the dam, where water with high CO_2 concentration was released from the hydropower reservoir, but decreased rapidly along the river as CO_2 was either released into the atmosphere or absorbed through photosynthesis. During peaks in hydropower activity, CO_2 concentration and emissions into the atmosphere increased rapidly, a phenomenon called "carbopeaking." The study highlights the importance of considering both natural and human sources of river CO_2 fluxes to fully understand the role of rivers in the carbon cycle and to predict their response to human activities and climate change.

1. Introduction

Rivers and streams play a fundamental role in the transport, processing, and exchange of organic and inorganic carbon along the river continuum (Battin et al., 2023). Unraveling and quantifying the processes that govern carbon fluxes along river networks is of paramount importance to understand and predict the response of the carbon cycle to global change. However, the drivers and dynamics of these fluxes are still largely unknown due to lack of data and inconsistent quantification approaches (Dean & Battin, 2024). Mountain rivers and streams, for instance, contribute disproportionately to global riverine greenhouse gas (GHG) emissions despite their relatively small surface area (Horgby, Segatto, et al., 2019). These rivers are characterized by high stream slopes, high turbulence intensities, and extensive occurrence of surface breaking and aeration. Overall, these factors yield higher gas transfer velocities and atmospheric exchange fluxes (Rocher-Ros et al., 2019; Ulseth et al., 2019), which are sustained by lateral inputs of organic and inorganic carbon and by the metabolic activity within the stream and across the watershed (Hotchkiss et al., 2015; Peter et al., 2014; Ulseth et al., 2018). The complex interplay between biogeochemical and geomorphological drivers induces a strong spatiotemporal variability of carbon and GHG fluxes across multiple scales, ranging from sub-diel (e.g., related to the ecosystem metabolism–Gomez-Gener et al. (2021)) and mesoscales (such as landscape-controlled hotspots—Rocher-Ros et al. (2019) and Duvert et al. (2018)) to seasonal and full catchment-scales variations (e.g., related to hydrological connectivity—Peter et al. (2014), Duvert et al. (2018), and Horgby, Boix Canadell et al. (2019)—and/or metabolic regimes: Schelker et al. (2016) and Bernhardt et al. (2018)). Such scale heterogeneity poses important challenges for the quantification of these fluxes (Ciais et al., 2014; Harmon, 2020).

In addition to "natural" drivers, the widespread regulation of rivers for hydropower energy production exerts additional controls on carbon and GHG fluxes (Silverthorn et al., 2023). The relatively long residence time in reservoirs supports strong metabolic activity which can promote large GHG concentrations depending on nutrients and oxygen availability (Hertwich, 2013; Maavara et al., 2020). As a result, increased dissolved GHG (e.g., CO_2, CH_4, and N_2O) concentrations and evasion fluxes are often observed in the rivers downstream of hydropower reservoirs (Galy-Lacaux et al., 1997; Guérin et al., 2006; Kemenes et al., 2016; Shi et al., 2023; Soued & Prairie, 2020). The fate of these additional GHG inputs depends on the physical and biogeochemical processes occurring along the river, which are affected by the design of the hydropower system and its operation. Hydropeaking is a widespread phenomenon resulting from the intermittent activation of the hydropower system according to energy market price and demand oscillations (Hauer et al., 2017; Hayes et al., 2023). The ensuing rapid fluctuations in flow discharge in the downstream reaches, sometimes accompanied by sudden variations in water temperature ("thermopeaking"—Toffolon et al. (2010) and Zolezzi et al. (2011)), oxygen (Winton et al., 2019) and/or total gas saturation ("saturopeaking"—Pulg et al. (2016)), have large impacts on the aquatic ecosystem, which can be detected for many kilometres downstream of the hydropower outlets (Hayes et al., 2022; Lennox et al., 2022; Moreira et al., 2019). The increase in water depth and turbidity during hydropeaking can also limit light availability at the stream bed, affecting primary productivity (Deemer et al., 2022; Hall et al., 2015). In contrast, environmental flow regulation can reduce flow variability and dampen floods, thereby enhancing ecosystem respiration and primary productivity (Aristi et al., 2014).

Recently, Calamita et al. (2021) recorded a temporary increment in CO_2 evasion during hydropeaking ("carbopeaking") downstream of a tropical reservoir (the Kariba Reservoir on the Zambezi River). Carbopeaking resulted from the combination of two factors: the higher CO_2 concentration in the hypolimnetic water that supplied the hydropower system; and the higher gas transfer rate coefficient due to stronger turbulence during hydropeaking. Carbopeaking, which occurs with sub-daily frequency, is not typically accounted for in the computation of the reservoir carbon budget.

Because of the strong spatiotemporal gradients and high localisation of GHG sources, the characterisation of GHG fluxes downstream of hydropower reservoirs is challenging, especially in Alpine rivers where the "natural" geomorphological and biochemical heterogeneity has been transformed by several centuries of anthropogenic pressure (Comiti, 2012), and where hydropower regulation is widespread. In this context, the use of diversion pipelines to connect a storage reservoir with a distant, lower-altitude, hydropower plant is a common approach for maximising the hydraulic head. In some cases, the by-passed river reach is regulated with a constant residual flow rate (baseflow). While the residual flow is still heavily affected by the presence of an upstream dam, the ecological impacts of hydropeaking dynamics are partially relieved (Bruno et al., 2023) and/or shifted downstream.

In light of the rapid ongoing transformation of the hydrology and biogeochemistry of mountain catchments driven by climate change (Boix Canadell et al., 2019; Brighenti et al., 2019; Hood et al., 2015) and of the boost in dam construction fueled by the increase in hydropower energy demand (Zarfl et al., 2015), understanding and quantifying the drivers of carbon and GHG fluxes (including the anthropogenic ones) is paramount to predict the role of the Alpine ecosystem for global carbon cycling and to inform suitable management actions. However, current measurement approaches are limited in their spatiotemporal resolution and coverage (Harmon, 2020), while numerical models suffer from a still incomplete description of the underlying processes (hence contributing to the epistemic uncertainty, *sensu* Beven and Westerberg (2011)) and from the dependence on a large number of parameters of influence, some of which are very difficult to determine (Battin et al., 2023).

Inverse modelling, that is, estimating the model parameters by fitting measured data, is a useful quantification approach to overcome at least in part these limitations (Saccardi & Winnick, 2021). The approach is often used for quantifying the ecosystem metabolism based on time series of dissolved oxygen concentration (Demars et al., 2015; Odum, 1956) also combined with CO_2 (Pennington et al., 2018). The extension to spatially resolved data has been proposed relatively recently to account for the spatial heterogeneity of physical and biological drivers. Segatto et al. (2023) developed a comprehensive framework to study fluxes of dissolved organic carbon and particulate organic carbon. Saccardi and Winnick (2021) employed a stream-network-scale model based on a steady-state one-dimensional CO_2 advection-reaction equation, quantifying groundwater inputs, runoff inputs, benthic hyporheic zone inputs, and water column respiration fluxes by optimising the fit with measurements. They neglected carbonate buffering, which can yield substantial effects in high-alkalinity waters (Stets et al., 2017). Winnick and Saccardi (2024) included carbonate buffering in the model of Saccardi and Winnick (2021), but they did not attempt a calibration with field data.

The objectives of this work are to understand and quantify the CO_2 fluxes and their drivers across multiple temporal scales in a regulated Alpine river by means of an inverse modelling approach. We conducted four extensive measurement campaigns during a year, covering the three main elements of a segment of a regulated Alpine river located in the Italian Alps: the upstream hydropower reservoir; two residual flow reaches; and a hydropeaking-affected reach. Then, we used the measured data to fit a one-dimensional, steady-state transport-reaction model to estimate the unknown terms of the CO_2 budget for this system: upstream and lateral inputs, ecosystem metabolism, atmospheric exchange, and carbonate buffering. With the aid of the model, we quantified the magnitude of these CO_2 inputs along the residual flow reaches, and compared them with the effects of carbopeaking observed downstream of the hydropower outlet. To our knowledge, this was the first application of inverse modelling applied to CO_2 fluxes that included the effects of carbonate buffering (speciation), motivated by the high alkalinity levels observed across our study site.

2. Methods

2.1. Study Site

We conducted multiple field measurement campaigns on the lower segment of the Noce River, the main right tributary of the Adige River, located in the Eastern Italian Alps. The Noce River is a fourth-order (Strahler stream order) highly-regulated Alpine stream with a total length of 105 km, that drains a catchment area of 1370 km^2 with river basin elevation ranging from 198 m a.s.l. (at the Adige River confluence) to 3,769 m a.s.l. (Mount Cevedale). The river is regulated for most of its length (DEE, 2022) and has been the subject of several studies regarding hydraulic, geomorphological, and biological alterations during hydropeaking (Bruno et al., 2009, 2010, 2023; Zolezzi et al., 2011). The present work focused on the lower segment of the river, downstream of the Santa Giustina reservoir (surface level 531.5 m a.s.l. at the maximum volume of 182.81×10^6 m^3 —DEE (2022)). This reservoir has been among the study sites of a previous work investigating near-surface CO_2 and CH_4 concentrations in 40 Alpine lakes and reservoirs (Pighini et al., 2018).

The Santa Giustina reservoir (from here on, upstream reservoir) feeds a cascade hydropower system through a diversion pipeline (see Figure 1): water abstracted from the upstream reservoir supplies an upstream power plant, and is released in the smaller Mollaro reservoir (from here on, intermediate reservoir; 348 m a.s.l. at the maximum volume of 0.85×10^6 m^3) approximately 6 km downstream, with a maximum flow rate during peak energy production of 66 m^3 s^{-1}; a second power plant at the bottom, fed by the intermediate reservoir and by two streams (rio Pongaiola and rio Rinassico), releases a maximum flow rate of 60 m^3 s^{-1} back into the Noce River through a 900 m long open channel (223 m a.s.l.). The two consecutive reaches stretching between the upstream reservoir and the hydropower outlet, separated by the intermediate reservoir, extend for an approximate total length of 18 km. They are regulated as residual flow (minimum flow) reaches supplied by two small turbines installed at the bottom of the upstream and intermediate dams, respectively. The prescribed minimum discharge varies throughout the year (2.6 m^3 s^{-1} in December to March; 3.2 m^3 s^{-1} in August and September; 3.7 m^3 s^{-1} for the rest of the year, DEE (2022)). Small tributaries contribute to an additional flow rate of ∼2.4–5.2 m^3 s^{-1} along the residual flow reaches (PAT, 2012). The reach downstream of the hydropower diversion outlet, extending for approximately 8 km until the confluence with the Adige River, is affected by hydropeaking. The average slope along the residual flow is 1.3% in the upstream reach (between the upstream reservoir and the intermediate

10.1029/2024WR037834

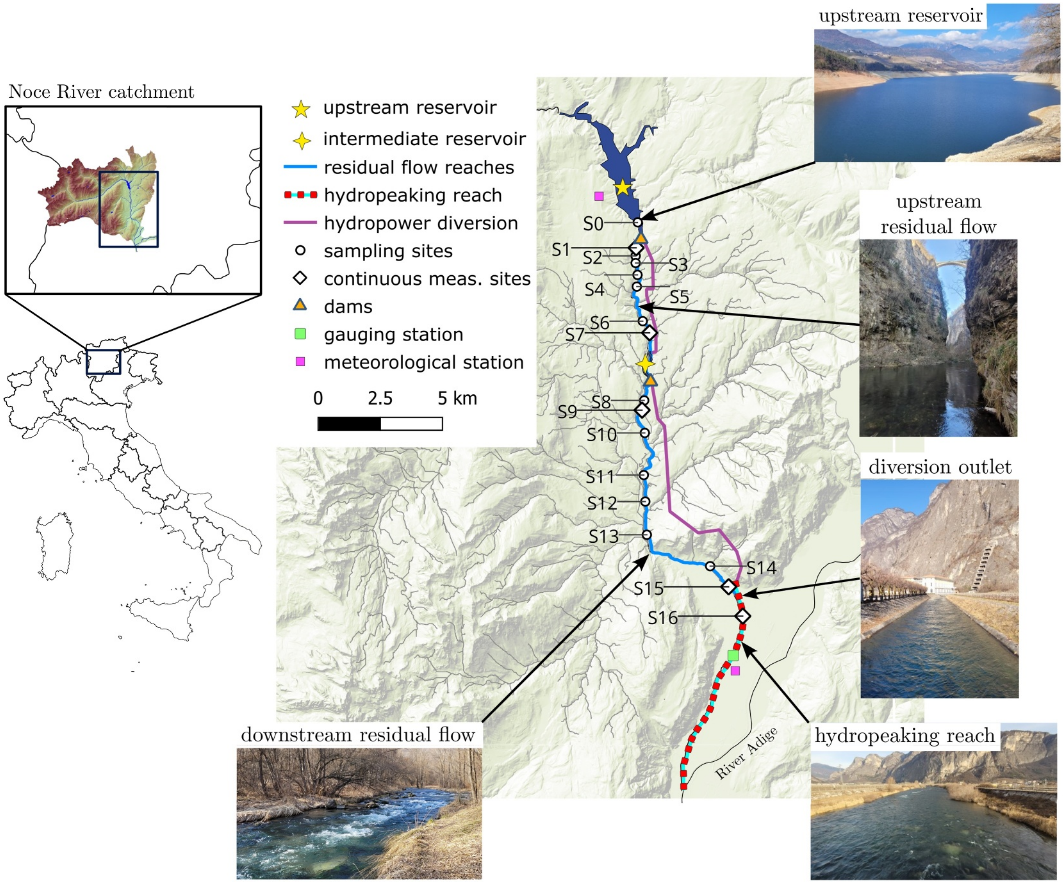

Figure 1. Map of the study site with the location of measurement sites and the outline of the three main components of the system, that is, the hydropower diversion system, the two residual flow reaches separated by the intermediate reservoir, and the hydropeaking-affected reach downstream of the hydropower diversion outlet.

reservoir), and 0.9% in the downstream reach (between the intermediate reservoir and the hydropower outlets), respectively. The average slope in the hydropeaking-affected reach is 0.4%.

2.2. Measurement Approach and Instrumentation

Field measurements and/or water sample collection were conducted at 17 sites in total (see Figure 1). Site S0 was located within the upstream reservoir, at a distance of approximately 0.65 km from the dam. The intermediate reservoir was not accessible for measurements. Seven measurement sites (S1 to S7) were distributed along the upstream residual flow reach, and eight measurement sites (S8 to S15) were distributed along the downstream residual flow reach. Site S16 was located along the hydropeaking-affected reach, 0.77 km downstream of the diversion outlet. Measurements were conducted during four separate campaigns: Mar23 (03-21 to 04-14-2023), Jun23 (06-13 to 06-22-2023), Aug23 (08-21 to 09-08-2023), and Nov23 (11-17 to 11-29-2023). The campaigns were distributed in such a way as to capture the main seasonal and climate patterns and reservoir stratification regimes. In particular, the Mar23 campaign followed a period of sustained lack of precipitation, while the Aug23 campaign was conducted a few days after a storm (85 mm of rain over 24 hr). The water level in the upstream reservoir changed by approximately 29 m throughout the period covered by the measurements, with the minimum depth (72 m at the sampling site) observed in Mar23 and the maximum depth (101 m) during Nov23 measurement campaign. The site S8 could only be accessed during Mar23 campaign.

2.2.1. Spot Measurements and Sample Analysis

Water samples (500 ml) were collected at sites S0 to S15 during the daytime. Samples along the residual flow (S1 to S15, one sample per site per campaign) were collected within the same day except for the Mar23 campaign when the sampling took two consecutive days. pH was measured directly with a calibrated analyzer, alkalinity was determined by titration, while CO_2 concentration was measured with the headspace method and further corrected for carbonate buffering (Koschorreck et al., 2020). Further details about the sample analysis and measurements uncertainties can be found in Text S1 of the Supporting Information S1. In the upstream reservoir (site S0), the samples were collected at multiple (11–13) depths using a Niskin bottle sampler. Vertical profiles of water temperature, salinity, conductivity, and chlorophyll *a* were measured using a MicroCTD profiler (Rockland Scientific, Canada). The vertical sampling and profiling covered the range from the water surface to less than 10 m above the bottom level.

2.2.2. Continuous Logging

Time series of $[CO_2]$, water level (D), water temperature (T_w), and incident light intensity (I_{light}) were recorded at five sites (S1, S7, S9, S15, and S16–see Figure 1) distributed along the two residual flow reaches and downstream of the diversion outlet. The measurements were conducted simultaneously at two sites at a time employing two individual sets of instruments. The instruments at sites S1, S7, and S9 recorded data with a sampling period of 15 min for at least 24 hr consecutively. A shorter sampling period (5 min) and longer duration (up to 72 hr) were employed at the most downstream sites S15 and S16 to capture the rapid flow variations driven by hydropeaking. Further details about the continuous measurements protocol and instrumentation can be found in Text S1 and Figure S1 of the Supporting Information S1.

2.2.3. Ancillary Meteorological and Hydraulic Data

Atmospheric pressure and air temperature data were retrieved from two meteorological stations operated by the Ufficio Previsioni e Organizzazione of the Autonomous Province of Trento located within 3 km from the hydropower diversion outlet (Mezzolombardo, Maso delle Part (MeteoTrentino stazioni meteorologiche, 2023)) and from the upstream dam (Cles, Maso Maiano (MeteoTrentino stazioni meteorologiche, 2003)), respectively. The flow rate was measured every 15 min at a gauging station managed by the Ufficio Dighe of the Autonomous Province of Trento (Mezzolombardo Ponte Rupe, PAT (2023)), located approximately 2.5 km downstream of the diversion outlet (1.6 km downstream of site S16, see Figure 1). The gauging data was used to estimate the flow rate, cross-section averaged flow velocity, and water depth at site S16 based on a set of custom rating curves (see Text S2, Supporting Information S1). The flow rate measured at the gauging station when the hydropower system was not operating (i.e., without hydropeaking) was defined as Q_{baseline}. Q_{baseline} varied from 6.0 $m^3\ s^{-1}$ for Mar23 data set to 10.0 $m^3\ s^{-1}$ for Nov23 data set.

Conditions inside the intermediate reservoir were unknown. Estimates of the representative values of $[CO_2]$, water temperature, pH, and TA were obtained through a weighted average of the fluxes entering the reservoir during a characteristic time duration τ_r related to the residence time of the intermediate reservoir. These fluxes were the inflow from the upstream residual flow reach, and the inflow from the upstream segment of the diversion system. The former was estimated based on measurements at site S7 (approximately 1.5 km upstream of the intermediate reservoir), while the latter was calculated according to measurements at site S16 assuming that the upstream and downstream hydropower plants operated synchronously and with the same flow rate in both segments of the diversion line. For the details of the calculation and the definition of the characteristic time duration τ_r see Text S3 in the Supporting Information S1.

2.2.4. CO_2 Evasion Fluxes

CO_2 evasion fluxes were modeled as follows (e.g., Wanninkhof, 1992):

$$F_{CO_2} = k\Delta, \tag{1}$$

where F_{CO_2} (mol $s^{-1}\ m^{-2}$) is the CO_2 flux intensity, k (m s^{-1}) is the gas-transfer rate,

$$\Delta = [CO_2] - [CO_2]_{\text{eq}} \tag{2}$$

is the CO_2 excess concentration, that is, the difference between the dissolved CO_2 concentration in water, $[CO_2]$ (mol m^{-3}), and the concentration that would be in equilibrium with the atmospheric CO_2 concentration, $[CO_2]_{\text{eq}}$.

10.1029/2024WR037834

The equilibrium concentration is evaluated as $[CO_2]_{eq} = K_0\, pCO_{2air}$ (mol m^{-3}), where pCO_{2air} (Pa) is the CO_2 partial pressure in air, and K_0 (mol l^{-1} Pa^{-1}) is the CO_2 solubility which depends on water temperature (Wanninkhof, 1992).

The distribution of the gas transfer rate k along the two residual flow reaches was estimated by fitting the measured $[CO_2]$ distribution using a 1D transport-reaction equation (see Section 2.3). In the reach subject to hydropeaking, this approach was not feasible due to rapid variations in flow rate and $[CO_2]$. There, k was quantified as $k = k_{600}(600/\mathrm{Sc})^{0.5}$, where k_{600} (m day^{-1}) is the gas transfer rate standardised to a Schmidt number of $\mathrm{Sc} = 600$. The Schmidt number, which represents the temperature-dependent ratio between water kinematic viscosity and mass diffusivity, was calculated according to Wanninkhof (1992). k_{600} was determined using the semi-empirical model of Ulseth et al. (2019),

$$\log(k_{600}) = \begin{cases} 3.10 + 0.35\log(\varepsilon_d), & \text{if } \varepsilon_d \le 0.018 \\ 6.43 + 1.18\log(\varepsilon_d), & \text{if } \varepsilon_d > 0.018 \end{cases}, \tag{3}$$

where $\varepsilon_d = g\,S\,V$ (m^2 s^{-3}) is the total specific stream power which approximates the turbulent kinetic energy dissipation rate (Moog & Jirka, 1999), g (m s^{-2}) is the gravity acceleration, S ($-$) is the bed slope, and V (m s^{-1}) is the mean flow velocity.

The model of Ulseth et al. (2019) was validated based on direct measurements (see Text S4 in Supporting Information S1) obtained with a CO_2 equilibration chamber mounted on a small anchored catamaran (Figure S1b in Supporting Information S1). The chamber was deployed at multiple sites and on multiple occasions: 15 measurements were conducted at site S16 with different flow rates; 8 measurements were conducted at 8 different locations within a distance of approximately 500 m from site S15, where the morphological units of the wet channel varied between runs and riffles (e.g., Parasiewicz, 2007). The conditions observed in the measurements were always within the high-energy stream range, with $\varepsilon_d > 0.018$ at all sites. The agreement between measured and predicted gas transfer rates (see Figure S2 in Supporting Information S1) was acceptable considering the large uncertainties of existing quantification approaches for k, especially in highly turbulent flows (Hall & Ulseth, 2020).

2.3. Transport-Reaction Model

The evaluation and quantification of the drivers of carbon and CO_2 fluxes were based on a 1D solute transport-reaction equation for the dissolved inorganic carbon concentration ([DIC]). The DIC and CO_2 concentration are linked through the definition of [DIC],

$$[\mathrm{DIC}] = [CO_2] + [HCO_3^-] + [CO_3^{2-}], \tag{4}$$

as the sum of the concentrations of CO_2 and of the main carbonate ion species. We did not account for calcite dissolution and precipitation, despite its potential relevance for Alpine rivers (Kanduč et al., 2012). Expressing the model in terms of DIC allows for considering carbonate buffering, that is, the variations in $[CO_2]$ caused by the shift in chemical equilibrium between the different DIC species. In high-alkalinity waters ($\sim$2 mmol l^{-1}), where the pool of ionized CO_2 (the carbonate buffer) is significant, the restoration of the chemical equilibrium dampens CO_2 variations driven by external drivers, that is, it delays atmospheric equilibration, reduces the intensity of atmospheric evasion fluxes, and limits the apparent primary productivity (Stets et al., 2017).

The DIC transport-reaction equation is derived from DIC balance along a well-mixed river cross-section subject to longitudinal advection, lateral inflow, atmospheric exchange, and stream metabolism (Pennington et al., 2018), and was adapted from Bencala and Walters (1983) neglecting dispersion:

$$\left(\frac{\partial}{\partial t} + \frac{Q}{A}\frac{\partial}{\partial x}\right)[\mathrm{DIC}] = \frac{q_L}{A}\left([\mathrm{DIC}]_L - [\mathrm{DIC}]\right) - \frac{W}{A}k\Delta - \frac{P_w}{A}\mathrm{NEP}, \tag{5}$$

where x (m) is the streamwise distance, t (s) is time, Q (m^3 s^{-1}) is the water flow rate, P_w (m) is the wetted perimeter, W (m) is the wet channel width, A (m^2) is the cross-sectional area, q_L (m^2 s^{-1}) is the lateral flow-rate

10.1029/2024WR037834

input per unit length, and $[\mathrm{DIC}]_L$ is the DIC concentration in the lateral inflow. NEP = GPP − ER (mol m^{-2} s^{-1}) represents the net ecosystem productivity, that is, the fixation and mineralization through gross primary production, GPP, and ecosystem respiration, ER, respectively. Throughout this work, NEP, GPP, and ER are expressed in moles of C. This contrasts with typical ecosystem metabolism estimates based on oxygen time series, which are commonly expressed in moles of oxygen. Unlike Saccardi and Winnick (2021), we did not distinguish between water column and hyporheic zone respiration fluxes, and we did not account for groundwater inputs explicitly. However, the lateral input term in Equation 5 can represent a generalized spatially distributed input from either surface water or groundwater, as long as q_L approximates the corresponding water exchange flux.

The excess CO_2 mass transport flux along the river reach is defined as

$$\phi_{\mathrm{CO_2}} = Q\Delta, \tag{6}$$

with units of mol s^{-1}. The relative importance of transport and evasion fluxes is represented by a turnover length scale Λ, defined as

$$\Lambda = \frac{1}{W}\frac{\phi_{\mathrm{CO_2}}}{F_{\mathrm{CO_2}}} = \frac{Q}{kW}. \tag{7}$$

Large values of Λ indicate that DIC is transported a long distance downstream with minimal interaction with the atmosphere. Small values of Λ are expected in turbulent mountain rivers where atmospheric exchange is predominant. Assuming steady state, introducing the definition of Λ from Equation 7, and approximating $P_w \approx W$ (wide cross-section), Equation 5 can be simplified as follows:

$$\Lambda\frac{\mathrm{d}}{\mathrm{d}x}[\mathrm{DIC}] = -\frac{q_L\Lambda}{Q}\left([\mathrm{DIC}] - [\mathrm{DIC}]_L\right) - \Delta - \frac{\mathrm{NEP}}{k}, \tag{8}$$

which is the equation used for inverse modeling in the residual flow reaches.

Λ has different physical meanings depending on the types of CO_2 sources and distribution. For instance, neglecting lateral inputs, metabolism, and carbonate buffering ($q_L = 0$, NEP = 0, and $\mathrm{d}[\mathrm{DIC}]/\mathrm{d}x = \mathrm{d}[\mathrm{CO_2}]/\mathrm{d}x$), and assuming $W = \mathrm{constant}$ for simplicity, the integration of Equation 8 yields

$$\Delta(x) = \Delta(x_0)\exp\left(-\frac{(x - x_0)}{\Lambda}\right), \tag{9}$$

that is, Λ represents the distance over which Δ approaches the asymptotic equilibrium $\Delta \to 0$ starting from an initial value $\Delta(x_0)$. Specifically, $\Delta(x)$ decreases by 63% relative to its initial value $\Delta(x_0)$ over a distance $(x - x_0) = \Lambda$ (i.e., $(\Delta(x) - \Delta(x_0))/\Delta(x_0) = 1 - \exp(-1) = 63\%$). If, instead, conditions are spatially homogeneous, for example, $q_L = 0$, $[\mathrm{DIC}] = \mathrm{const.}$, then $\Delta = -\mathrm{NEP}/k$, and

$$\Lambda = \frac{Q\Delta}{Wk\Delta} = -\frac{Q\Delta}{W\,\mathrm{NEP}}, \tag{10}$$

that is, Λ represents the "turnover distance" which is required by an initial CO_2 pool (represented by an upstream flux $Q\Delta$ (mol s^{-1})) to be fully depleted to the atmosphere through evasion fluxes, ($\Lambda Wk\Delta$, mol s^{-1}), and replaced with an equal amount of CO_2 originating from the ecosystem metabolism ($\Lambda W\mathrm{NEP}$, mol s^{-1}).

Substituting k from Equations 3 into 7, Λ can be related to the flow velocity and turbulent kinetic energy dissipation rate, revealing a different behavior for low-energy and high-energy streams. Assuming Sc is constant and generalizing Equation 3 in the form $k = b(\varepsilon_d)^a$, ($a = 0.35$ when $\varepsilon_d \leq 0.018$ and $a = 1.18$ when $\varepsilon_d \geq 0.018$), one finds

$$\Lambda^* = \frac{\Lambda}{D} = \frac{V}{k} \sim \frac{1}{b(gS)^a}V^{(1-a)}, \tag{11}$$

where Λ^* is the non-dimensionalized Λ based on an equivalent average water depth $D = Q/(VW)$. If $S =$ constant and $\varepsilon_d > 0.018$, the exponent of V is negative and an increase in flow velocity is associated with a decrease in Λ^*, that is, a larger relative weight of evasion fluxes compared to transport fluxes, and a more rapid turnover. In this case, the sensitivity of Λ^* to variations in V is rather small, $\Lambda^* \sim V^{-0.18}$ (see Figure S3 in the Supporting Information S1). If $\varepsilon_d < 0.018$ the exponent of V is positive, therefore, increasing the flow velocity yields an increase in Λ^*, meaning a longer non-dimensional travel distance before reaching equilibrium. An increase in river slope S is always associated with a decrease in Λ^* if the average flow velocity remains constant.

2.4. Data Interpretation Through the Model

We used Equation 8 for quantifying the magnitude of the main contributors to the CO_2 mass balance along the residual flow reaches. A similar approach was used previously by Saccardi and Winnick (2021) to reconstruct CO_2 dynamics at watershed scales neglecting carbonate buffering. Following these authors, the ordinary differential equation (Equation 8) was approximated and solved numerically on a uniform grid (50 m resolution) using a first-order forward difference scheme.

The integration was conducted along two separate computational domains representing the upstream ($x_0^{(us)}$, $x_1^{(us)}$, … $x_{end}^{(us)}$) and downstream $\left(x_0^{(ds)}, x_1^{(ds)}, \dots x_{end}^{(ds)}\right)$ residual flow reaches, respectively. The upstream domain had a length of $L^{(us)} = 6$ km (121 nodes) and extended from the upstream dam $\left(x_0^{(us)}\right)$ to the confluence of the upstream residual flow reach into the intermediate reservoir $\left(x_{end}^{(us)}\right)$. The downstream residual flow domain had a length of $L^{(ds)} = 11.6$ km (233 nodes) and extended from the intermediate dam $\left(x_0^{(ds)}\right)$ to the outlet of the hydropower diversion system $\left(x_{end}^{(ds)}\right)$. The wet channel width was assumed constant within each reach, since the differences associated with width variations were estimated to be negligible (see Text S5 of the Supporting Information S1). Within both domains, the flow rate $Q(x_i)$ at the i-th node was assumed to be proportional to the drainage area upstream of the node, $\mathrm{DA}_i(x_i)$ (m^2), following Conroy et al. (2023),

$$Q(x_i) = Q\left(x_0^{(us)}\right) + \left[Q_{baseline} - Q\left(x_0^{(us)}\right)\right] \frac{\mathrm{DA}_i(x_i)}{\mathrm{DA}_g}, \tag{12}$$

where DA_g (m^2) was the drainage area calculated at the location of the gauging station (located in the reach subject to hydropeaking), $Q_{baseline}$ was the baseline discharge measured at the gauging station in the absence of hydropeaking, and $Q\left(x_0^{(us)}\right)$ was equal to the minimum permissible residual flow discharge. q_L was calculated as

$$q_L(x_i) = \frac{Q(x_i) - Q(x_{i-1})}{x_i - x_{i-1}}. \tag{13}$$

[DIC], [CO_2], pH, and TA are related by chemical equilibrium relations, which allow the calculation of any of these quantities if at least two of them are known (Dickson et al., 2007). Since the integration was conducted with respect to [DIC], either [CO_2], pH, or TA should have been determined iteratively. To reduce the computational effort we avoided iterating by prescribing the conservation of total alkalinity in the form

$$Q(x_i)\,\mathrm{TA}(x_i) = Q(x_0)\,\mathrm{TA}_0 + \sum_{j=1}^{i} (x_j - x_{j-1})\, q_L(x_j)\, \mathrm{TA}_L, \tag{14}$$

where TA_L was the total alkalinity in the lateral inflow, which was assumed to be constant in space, and $\mathrm{TA}_0 = \mathrm{TA}(x_0)$ was the TA at the upstream boundary of each reach. The assumption was justified by the fact that variations in CO_2 do not affect alkalinity, and variations in TA due to nutrient uptake or mineralization are small (Stets et al., 2017; Winnick & Saccardi, 2024).

Temporal variations were neglected by assuming steady-state conditions for each quantity in Equation 5, including the NEP. This was made possible by considering only the behavior at peak daytime (when GPP reaches its maximum) and nighttime (when GPP $= 0$), separately, that is,

$$\mathrm{NEP}_{\mathrm{peak,day}} = \mathrm{GPP}_{\mathrm{peak}} - \mathrm{ER}, \tag{15}$$

$$\mathrm{NEP}_{\mathrm{peak,night}} = 0 - \mathrm{ER}. \tag{16}$$

Such an approximation was acceptable in the residual flow reaches because NEP variations occurred on a temporal scale significantly larger than the time required for the system to reach equilibrium. In fact, applying a dimensional analysis to Equation 5, neglecting lateral inputs and carbonate buffering for simplicity, the timescale to reach equilibrium can be estimated as Λ/V, which corresponds to the time required for a parcel of water to travel a distance Λ. During this time, the whole CO_2 pool is renewed and the system loses memory of previous changes. We estimated $\Lambda/V \approx 40$ minutes, which was fast compared to NEP fluctuations occurring over multiple hours.

Λ and the other parameters of Equation 8 were estimated by fitting the model predictions and the measured distributions of $[CO_2]$, pH, TA, and [DIC]. Details of the procedure and calculation of the model parameter uncertainties are discussed in Text S5 of the Supporting Information S1. The T_w distribution was calculated separately for each data set by fitting an exponential function of the type $T_w(x_i) = T_w(x_0) + c_2 \exp((x_i - x_0)/c_3)$. Nine additional parameters were estimated based on Equations 8 and 14–16: the upstream boundary values of [DIC] and TA ($[\mathrm{DIC}]_0^{(\mathrm{us})}$ and $\mathrm{TA}_0^{(\mathrm{us})}$ in the upstream reach, $[\mathrm{DIC}]_0^{(\mathrm{ds})}$ and $\mathrm{TA}_0^{(\mathrm{ds})}$ in the downstream reach); the DIC concentration and TA of the lateral inflow ($[\mathrm{DIC}]_L$ and TA_L, respectively); the daytime and nighttime $\mathrm{NEP}_{\mathrm{peak}}$ ($\mathrm{NEP}_{\mathrm{peak,day}}$ and $\mathrm{NEP}_{\mathrm{peak,night}}$, respectively); and Λ. Except for Λ which was assumed to be constant throughout, each parameter was allowed to change across measurement campaigns. $\mathrm{NEP}_{\mathrm{peak}}$ changed from daytime to nighttime according to Equations 15 and 16, while the other parameters were assumed to be independent of the time of day. Λ, $[\mathrm{DIC}]_L$, TA_L, $\mathrm{NEP}_{\mathrm{peak,day}}$ and $\mathrm{NEP}_{\mathrm{peak,night}}$ were represented by single average values representative of the two reaches. The choice of limiting the variability of the parameters in space and/or time in such a way was driven by the limited size of the data set, and followed a similar approach in previous studies to mitigate the potential impacts of equifinality on the uncertainty of the estimated parameters (Conroy et al., 2023; Saccardi & Winnick, 2021). In the case of Λ, fixing a unique representative value for all data sets was justified by the small variability of Λ^* for high-energy flows such as the one in the residual flow. Local values of k were calculated from the estimated values of Λ and Q. In this way, we were able to account for k variability in space and across data sets in a physically realistic way with a relatively small number of degrees of freedom.

2.5. Calculation of CO_2 Inputs in the Residual Flow Reaches

We employed the model of Equation 8 calibrated with measurements to calculate the magnitude of the main CO_2 fluxes along the residual flow reaches. Positive fluxes were used to represent inputs of CO_2 into the system. We distinguished seven main contributions to the budget of CO_2: ecosystem metabolism (EM), upstream influx (IN), downstream export (OUT), lateral inputs (LAT), surface exchange (SURF), and carbonate buffering (CHEM).

$$\mathrm{EM} = -\left(W^{(\mathrm{us})}L^{(\mathrm{us})} + W^{(\mathrm{ds})}L^{(\mathrm{ds})}\right)\mathrm{NEP}_{\mathrm{peak}} \tag{17}$$

represents the CO_2 production by the ecosystem metabolism (mol/s). EM is positive during the night but can be negative during the day if primary production dominates over respiration.

We expressed CO_2 transport fluxes in terms of the flux of "excess" CO_2, Δ, obtained through the decomposition $[CO_2] = [CO_2]_{\mathrm{eq}} + \Delta$, to highlight the processes that shift CO_2 concentration away from equilibrium:

$$\mathrm{IN} = Q\left(x_0^{(\mathrm{us})}\right)\Delta\left(x_0^{(\mathrm{us})}\right) - Q\left(x_{\mathrm{end}}^{(\mathrm{us})}\right)\Delta\left(x_{\mathrm{end}}^{(\mathrm{us})}\right) + Q\left(x_0^{(\mathrm{ds})}\right)\Delta\left(x_0^{(\mathrm{ds})}\right) \tag{18}$$

represents the net excess CO_2 input from the upstream and intermediate dams into both residual flow reaches, where $x_0^{(\mathrm{us})}$ and $x_0^{(\mathrm{ds})}$ are the upstream and intermediate dam locations, respectively, and $x_{\mathrm{end}}^{(\mathrm{us})}$ represents the intermediate reservoir confluence location. The CO_2 concentration inside the intermediate reservoir depends on (a) the input from the upstream reservoir through the diversion system and (b) the input from the upstream reach at the confluence, approximated with $Q\left(x_{\text{end}}^{(\text{us})}\right)\Delta\left(x_{\text{end}}^{(\text{us})}\right)$. This last term has been subtracted in Equation 18 to isolate the contribution from the hydropower system.

$$\text{OUT} = -Q\left(x_{\text{end}}^{(\text{ds})}\right)\Delta\left(x_{\text{end}}^{(\text{ds})}\right) \tag{19}$$

represents the excess CO_2 outflow at the downstream end of the residual flow, $x_{\text{end}}^{(\text{ds})}$, located directly upstream of the diversion pipeline outlets. According to our sign convention, an outflow of undersaturated water $\left(\Delta\left(x_{\text{end}}^{(\text{ds})}\right) < 0\right)$ resulted in $\text{OUT} > 0$, which indicates an apparent input of CO_2 into the system. This is a direct consequence of our choice to represent fluxes in terms of Δ, and it bears a physical meaning: since both water and CO_2 mass are conserved, the outflow of water with low CO_2 concentration yields an increase in average CO_2 concentration in the system.

$$\text{LAT} = \sum_{i=0}^{\text{end}} \left(x_i^{(\text{us})} - x_{i-1}^{(\text{us})}\right) q_L\left(x_i^{(\text{us})}\right)\Delta_L\left(x_i^{(\text{us})}\right) + \sum_{i=0}^{\text{end}} \left(x_i^{(\text{ds})} - x_{i-1}^{(\text{ds})}\right) q_L\left(x_i^{(\text{ds})}\right)\Delta_L\left(x_i^{(\text{ds})}\right) \tag{20}$$

represents the lateral input of excess CO_2, where Δ_L was the excess CO_2 concentration in the lateral inflow calculated based on $[\text{DIC}]_L$ and TA_L. $\text{LAT} < 0$ when $\Delta_L < 0$.

$$\text{SURF} = -\sum_{i=0}^{\text{end}} \left(x_i^{(\text{us})} - x_{i-1}^{(\text{us})}\right) k\left(x_i^{(\text{us})}\right)\Delta\left(x_i^{(\text{us})}\right) W^{(\text{us})} - \sum_{i=0}^{\text{end}} \left(x_i^{(\text{ds})} - x_{i-1}^{(\text{ds})}\right) k\left(x_i^{(\text{ds})}\right)\Delta\left(x_i^{(\text{ds})}\right) W^{(\text{ds})} \tag{21}$$

represents the CO_2 exchange with the atmosphere. $\text{SURF} < 0$ indicates a flux of CO_2 from water toward the atmosphere.

The CO_2 balance in the residual flow is closed with the input of CO_2 due to carbonate buffering. We calculated it in terms of the net imbalance of HCO_3^- and CO_3^{2-}:

$$\text{CHEM} = \text{IN}_{HCO_3^-} + \text{IN}_{CO_3^{2-}} + \text{LAT}_{HCO_3^-} + \text{LAT}_{CO_3^{2-}} + \text{OUT}_{HCO_3^-} + \text{OUT}_{CO_3^{2-}}. \tag{22}$$

2.6. Carbopeaking Quantification in the Hydropeaking-Affected Reach

The CO_2 inputs described in Section 2.5 refer to the residual flow reaches and were calculated by fitting Equation 8 to the measured data. To compare the magnitude of these inputs with the effects of carbopeaking, we expressed the latter in terms of the average increase in excess CO_2 mass influx in the hydropeaking-affected reach during hydropeaking, as follows:

$$\text{CPeak} = \langle Q(x_{\text{HP}}, t_j)\Delta(x_{\text{HP}}, t_j)\rangle_{\text{HP}} + \text{OUT}, \tag{23}$$

where $Q(x_{\text{HP}}, t_j)\Delta(x_{\text{HP}}, t_j) = \phi_{CO_2}(x_{\text{HP}}, t_j)$ indicates the instantaneous excess CO_2 mass flow rate measured at the location of the diversion outlet, x_{HP}, and $\langle\cdot\rangle_{\text{HP}}$ denotes conditional averaging during hydropeaking events. In practice, we approximated $Q(x_{\text{HP}}, t_j)\Delta(x_{\text{HP}}, t_j)$ with the product of the measured Q and Δ time-series recorded at site S16. The addition of the term OUT is to subtract the baseline CO_2 flux coming from the residual flow reaches and to isolate the increase due to carbopeaking.

We defined the relative increase in average Δ during hydropeaking as

$$\delta_\Delta = \frac{\langle\Delta(x_{\text{HP}}, t_j)\rangle_{\text{HP}} - \left\langle\Delta\left(x_{\text{end}}^{(\text{ds})}, t_j\right)\right\rangle}{\left\langle\Delta\left(x_{\text{end}}^{(\text{ds})}, t_j\right)\right\rangle}, \tag{24}$$

where $\left\langle\Delta\left(x_{\text{end}}^{(\text{ds})}, t_j\right)\right\rangle$ was the time average of Δ at site S15. The quantities δ_Q and δ_k, calculated in a similar way, indicated the relative increase in Q and k during hydropeaking. We chose to quantify hydropeaking-related variations based on conditional averaging rather than based on time derivatives (as done by Calamita

10.1029/2024WR037834

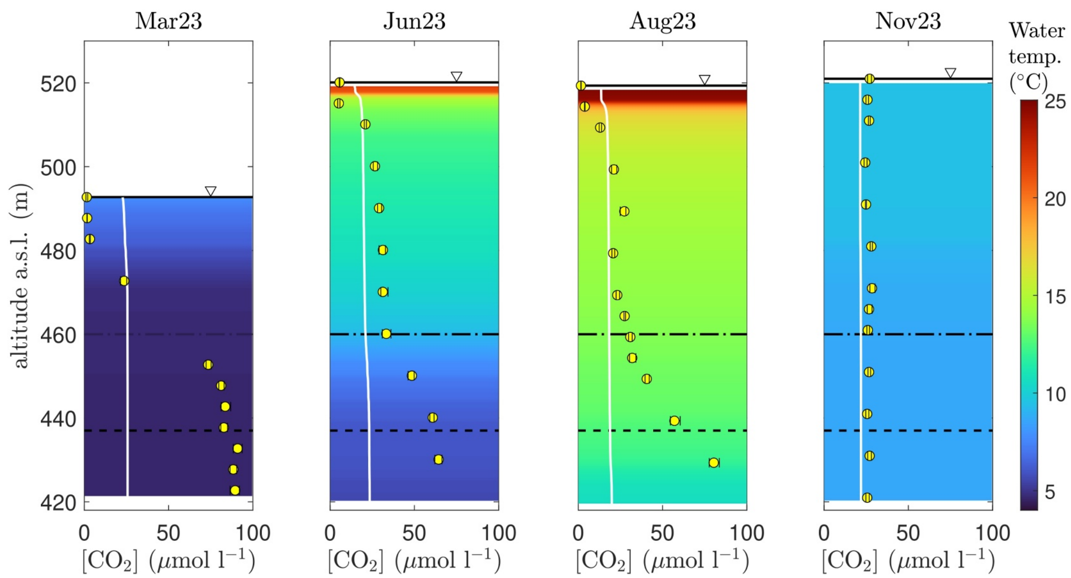

Figure 2. Profiles of sampled dissolved CO_2 concentration $[CO_2]$ (circles) and measured water temperature T_w (colormap) in the upstream reservoir during the four measurement campaigns. The vertical segments near each circle represent the measurement uncertainties. White line: calculated equilibrium concentration, $[CO_2]_{eq}$. Dashed line: diversion system intake level. Dashed-dotted line: residual flow intake level.

et al. (2021)) to mitigate the impact of random signal noise on the calculation. As in Calamita et al. (2021), the relative contribution of k and Δ variations to the increase in F_{CO_2} during hydropeaking were approximated as $\delta_k/(\delta_k + \delta_\Delta)$ and $\delta_\Delta/(\delta_k + \delta_\Delta)$, respectively. The relative contribution of Q and Δ variations to the increase in ϕ_{CO_2} during hydropeaking were approximated as $\delta_Q/(\delta_Q + \delta_\Delta)$ and $\delta_\Delta/(\delta_Q + \delta_\Delta)$, respectively.

3. Results

3.1. Measurements in the Upstream Reservoir

The profiles of CO_2 concentration and water temperature measured at site S0 in the upstream reservoir (Figure 2) displayed a marked seasonal variability. The $[CO_2]$ was higher at larger depths and lower near the water surface, except during Nov23 campaign when it was approximately uniformly distributed following lake overturning. The depth-averaged CO_2 concentration varied between a minimum of 26 μmol/l during Nov23 campaign and a maximum of 53 μmol/l during Mar23 campaign. To highlight the potential evasion flux upon release into the river, $[CO_2]_{eq}$ was calculated at every depth based on the local water temperature and average atmospheric CO_2 concentration ($pCO_{2\mathrm{air}} = 425$ ppm) at atmospheric pressure, without considering pressure variations with depth inside the reservoir. As a result, water was consistently supersaturated at the two intakes of the hydropower diversion system and of the penstock that fed the residual flow reaches.

Except for Nov23, values of $[CO_2]$ near the water surface were well below the equilibrium concentration, causing an influx of CO_2 from the atmosphere according to Equation 1. Near the surface, the decrease in $[CO_2]$ was accompanied by an increase in chlorophyll *a* (see Figure S4 in the Supporting Information S1), suggesting that the undersaturation near the surface was driven by the activity of primary producers such as planktonic algae blooming in the upper layers of the reservoir. The primary productivity in the reservoir was not quantified, as the low turbulent mixing in the reservoir increased the response time of the $[CO_2]$ loggers affecting the uncertainty of temporal $[CO_2]$ variations. Throughout all data sets, the measured pH was between 7.4 and 9.3, while the measured total alkalinity varied between 1.3 and 2.2 mmol l^{-1} (Figures S5 and S6 of the Supporting Information S1).

3.2. Measurements Along the Residual Flow

Temporal variations in $[CO_2]$ and T_w (Figures 3 and S7, respectively) at the continuous monitoring sites S1, S7, S9, and S15 along the residual flow reaches, displayed a significant diel variability, with lower daytime $[CO_2]$

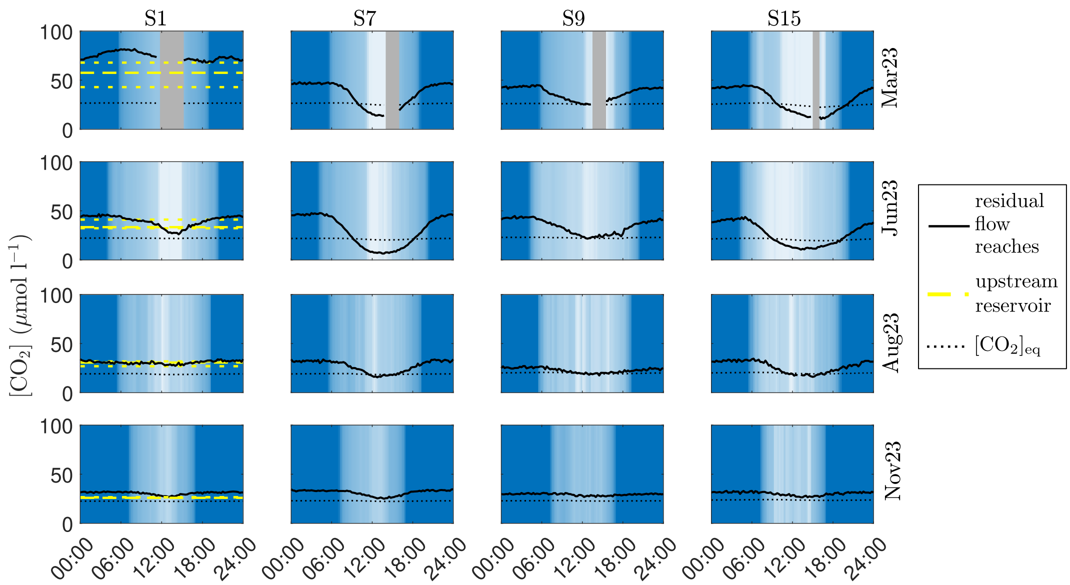

Figure 3. Measured time series of $[CO_2]$ along the residual flow (sites S1, S7, S9, S15) as a function of the time of day. Solid, black: measured $[CO_2]$ in the residual flow reaches. Dotted, black: calculated $[CO_2]_{eq}$. Dashed, yellow: sampled $[CO_2]$ in the upstream reservoir at the residual flow intake level (dotted lines bind the uncertainty interval). Background colors represent the logarithm of the measured light intensity (the dark blue color indicates nighttime). Gray-shaded regions indicate periods for which measurements were not available.

levels indicating the effects of primary production (e.g., Peter et al., 2014). Diel variations in $[CO_2]$ were clearly visible at sites S7 and S15 located furthest downstream from the upstream and intermediate dams, respectively. The peak-to-peak $[CO_2]$ range was very small during Nov23 campaign and was largest during Mar23 and Jun23 campaigns, when water became undersaturated $\left([CO_2] < [CO_2]_{eq}\right)$ during the daytime. The range was somewhat reduced at site S9 downstream of the intermediate dam, while variations were almost absent at site S1 closest to the upstream dam. The daily average of CO_2 excess concentration Δ was positive at all sites and varied between 2.94 μmol l^{-1} (at site S9 for Aug23 data set) and 47.38 μmol l^{-1} (at site S1 for Mar23 data set). The highest instantaneous value of $\Delta = 54.90$ μmol l^{-1} was observed at 8:00 at site S1 for Mar23 data set, while the lowest value of $\Delta = -13.85$ μmol l^{-1} was observed at 13:50 at site S7 for Jun23 data set.

The daytime spatial distributions of T_w and Δ measured at the sampling sites S1 to S15 (Figures 4a and 4b) indicated a decrease in Δ and an increase in T_w (except for Nov23 data set) with the distance from the upstream dam, driven by lower CO_2 concentrations and higher air temperature in the atmosphere compared to the hypolimnetic water in the upstream reservoir (see Figure S8 in Supporting Information S1). The decay in Δ occurred rapidly within a distance of approximately 2 km from the upstream dam, between sites S1 and S5, and was likely driven by the combined effects of atmospheric evasion and primary production. Beyond site S5, Δ showed limited spatial variation within each data set, but a clear variability across different data sets. During the day, water was undersaturated in CO_2 ($\Delta < 0$) for Mar23, Jun23, and Aug23 data sets, and supersaturated ($\Delta > 0$) for Nov23 data set. The lowest values of Δ were observed for Mar23 and Jun23 data sets. The pH distribution (Figure 4c) mirrored the distribution of Δ as a consequence of chemical equilibrium. Total alkalinity (Figure 4d) varied between 1.2 and 2.9 mmol l^{-1} and increased along the residual flow most likely because of lateral influx from the watershed. The maximum in TA occurred during Nov23 campaign, although the strongest spatial variation in TA along the residual flow was observed during Aug23 campaign.

3.3. Model Fitting Along the Residual Flow

We obtained an estimate of the nine unknown parameters Λ, $NEP_{peak,day}$, $NEP_{peak,night}$, $[DIC]_L$, $[DIC]_0^{(us)}$, $[DIC]_0^{(ds)}$, TA_L, $TA_0^{(us)}$, and $TA_0^{(ds)}$ by fitting the data measured along the residual flow reaches by means of Equations 8 and 14–16. The comparison between measured data distributions and model predictions are shown in Figure 5 for the Jun23 data set and in Figures S9, S10, and S11 in Supporting Information S1 for the Mar23,

10.1029/2024WR037834

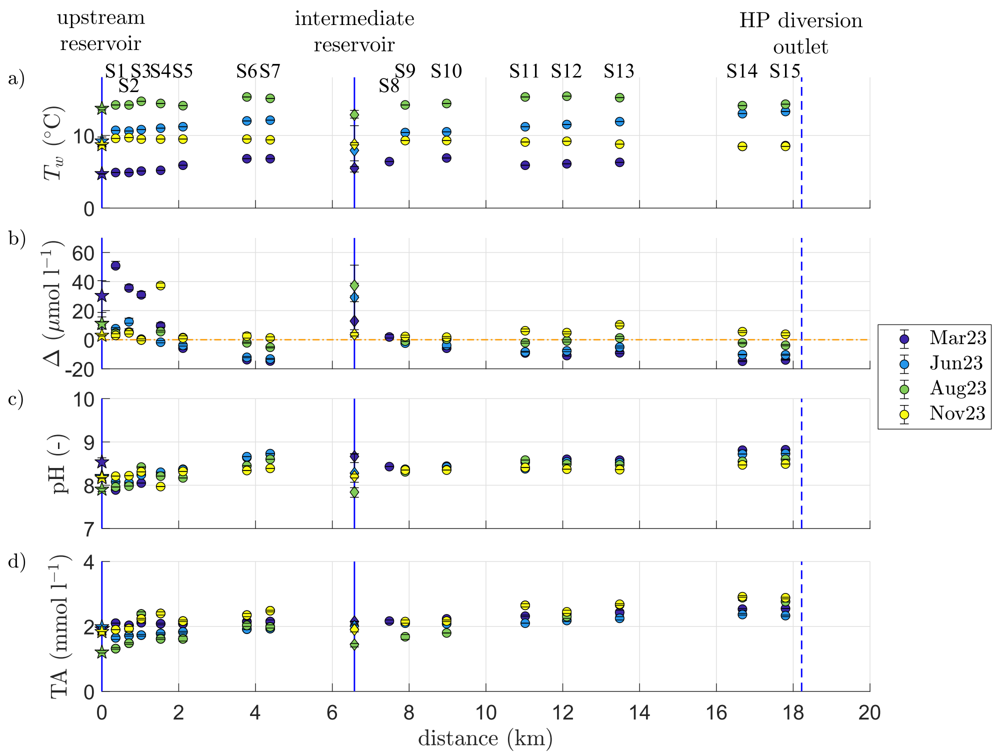

Figure 4. Spatial daytime distributions along the residual flow of measured (a) water temperature, T_w, (b) excess CO_2 concentration, Δ, (c) pH, and (d) total alkalinity, TA, as a function of the distance from the upstream dam. Daytime measurements are representative of the daily minimum CO_2 concentrations (see Figure 3) and maximum water temperatures at each site. Circles: sample measurements (the horizontal segments represent the measurement uncertainties); stars: measurements at the residual flow intake inside the upstream reservoir; diamonds: average values inside the intermediate reservoir based on the weighted average of the input fluxes (see Text S3 in Supporting Information S1) (the horizontal segments indicate diel minima/maxima); orange dashed-dotted line: atmospheric equilibrium conditions, $\Delta = 0$; solid blue lines: location of the upstream (0 km) and intermediate (6.6 km) dams; dashed blue line: location of the hydropower diversion outlet (18.2 km).

Aug23, and Nov23 data sets, respectively. The fitted model parameters are reported in Table 1. The estimated levels of TA_L and $[DIC]_L$ (up to 5 mmol l^{-1}) were consistent with the scenarios considered by Winnick and Saccardi (2024) based on the range observed across streams in the United States (Stets et al., 2017). Λ was estimated to be approximately 2.5 km, which was consistent with the rapid equilibration of Δ observed close downstream of the dams in Figure 4. Local values of k were calculated at each grid location based on $Q(x_i)$ and estimated Λ. The spatial average of k varied between 7.2 m d^{-1} for Aug23 data set in the upstream reach and 17.2 m d^{-1} for Nov23 data set in the downstream reach, in agreement with the direct measurements at site S15 (Figure S2 in Supporting Information S1). The higher estimated k in the downstream reach compared to the upstream reach was consistent with the increase in flow rate along the residual flow reaches.

The estimated CO_2 inputs along the residual flow reaches, calculated according to Section 2.5 and summarized in Figure 6, reveal different dominant drivers at different times of the year. The magnitude of atmospheric CO_2 exchange (SURF) was largest during the Jun23 campaign (0.34 mol s^{-1} during the day and −0.79 mol s^{-1} during the night; negative input values indicate a decrease in riverine CO_2 stock, i.e., evasion to the atmosphere). The residual flow was a sink of atmospheric CO_2 during the day, and a source during the night, except for Nov23 campaign. The magnitude of nighttime evasion intensities was always higher than the daytime intake from the atmosphere. The net input from the dams (IN) was significantly smaller for Nov23 data set during lake overturning (−0.04 mol s^{-1} to 0.00 mol s^{-1}) compared to the other data sets (0.01 mol s^{-1} to 0.26 mol s^{-1}). Lateral inputs (LAT) (−0.05 to 0.05 mol s^{-1}) were consistently small. Positive downstream transport (OUT) observed at daytime between Mar23 and Aug23 indicates outflow of undersaturated water ($\Delta < 0$).

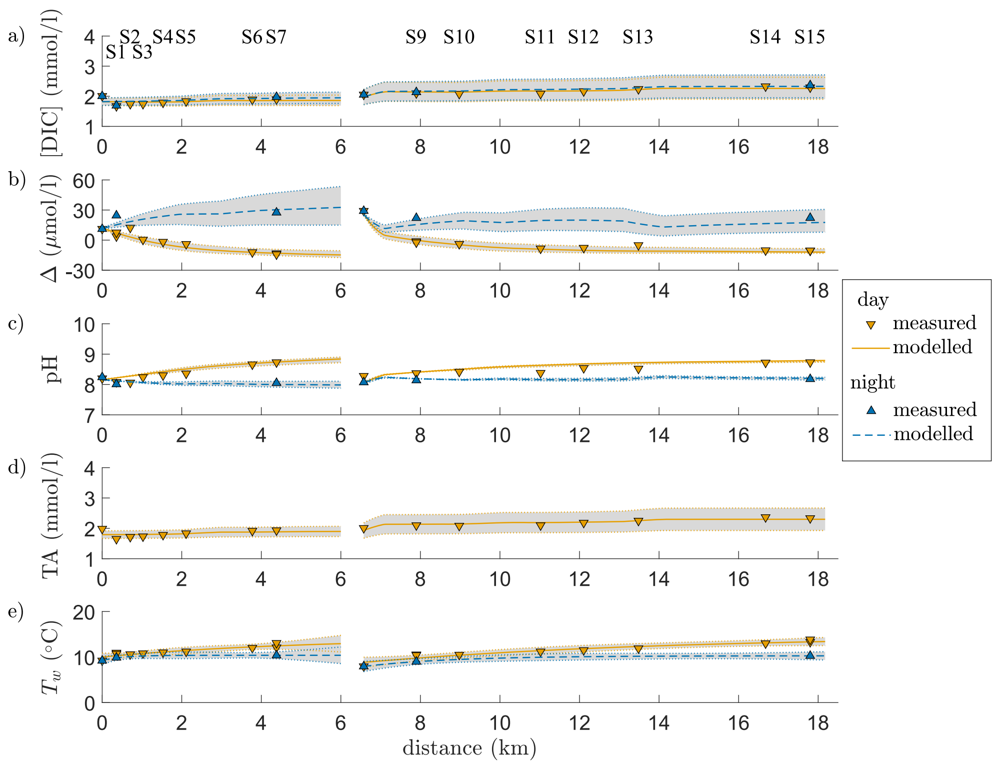

Figure 5. Example of modeled (lines) and measured (triangles) parameters distribution along the residual flow, based on Jun23 data set. The gray shaded areas indicate 95% confidence intervals according to fitting uncertainties. (a): DIC concentration, [DIC]; (b): CO_2 excess concentration, Δ; (c) pH; (d): total alkalinity, TA; (e): water temperature, T_w.

Metabolic drivers (EM) were predominant during all campaigns, especially for Jun23 data set (−0.97 mol s^{-1} during the day and 1.11 mol s^{-1} during the night). Daytime EM was negative for Mar23, Jun23, and Aug23 data sets (ER<GPP_{peak}). In Aug23 during daytime, the magnitude of EM was much smaller (−0.13 mol s^{-1}), but the

Table 1
CO_2 *Model Parameters Along the Residual Flow Reaches*

		Mar23	Jun23	Aug23	Nov23
Estimated parameters	ER (μmol m^{-2} s^{-1})	1.89 ±1.08	3.91 ±1.20	2.15 ±0.77	1.73 ±0.99
	GPP_{peak} (μmol m^{-2} s^{-1})	5.59 ±1.74	7.30 ±2.14	2.62 ±1.34	1.23 ±1.66
	$DIC_0^{(us)}$ (mmol l^{-1})	2.09 ±0.12	1.82 ±0.12	1.57 ±0.12	2.07 ±0.13
	$DIC_0^{(ds)}$ (mmol l^{-1})	2.09 ±0.24	1.97 ±0.25	1.26 ±0.25	1.75 ±0.26
	DIC_L (mmol l^{-1})	4.12 ±1.26	2.64 ±0.49	4.68 ±0.58	3.63 ±0.40
	$TA_0^{(us)}$ (mmol l^{-1})	2.02 ±0.12	1.79 ±0.13	1.55 ±0.13	2.05 ±0.13
	$TA_0^{(ds)}$ (mmol l^{-1})	2.06 ±0.24	1.93 ±0.25	1.20 ±0.25	1.73 ±0.26
	TA_L (mmol l^{-1})	4.08 ±1.27	2.68 ±0.49	4.82 ±0.58	3.64 ±0.41
	Λ (km)	2.53 ±0.87	2.53 ±0.87	2.53 ±0.87	2.53 ±0.87
Derived parameters	$k^{(us)}$ (m d^{-1})	$8.1^{+4.3}_{-2.1}$	$8.6^{+4.5}_{-2.2}$	$7.2^{+3.8}_{-1.9}$	$8.8^{+4.6}_{-2.3}$
	$k^{(ds)}$ (m d^{-1})	$9.7^{+5.1}_{-2.5}$	$14.6^{+7.7}_{-3.8}$	$11.2^{+5.9}_{-2.9}$	$17.2^{+9.0}_{-4.4}$
	F_{CO_2} (μmol m^{-2} s^{-1}) (day)	$-1.2^{+0.9}_{-1.5}$	$-2.2^{+1.2}_{-1.9}$	$-0.6^{+0.7}_{-1.1}$	$1.1^{+0.5}_{-0.7}$
	F_{CO_2} (μmol m^{-2} s^{-1}) (night)	$4.7^{+0.7}_{-0.9}$	$5.4^{+0.7}_{-0.9}$	$2.0^{+0.6}_{-0.8}$	$2.4^{+0.7}_{-0.9}$

Note. The estimated parameters are the outputs of the optimisation, while the derived parameters k and F_{CO_2} were calculated based on Equations 1 and 7, respectively. The values of k reported here are the spatial averages calculated for each residual flow reach. F_{CO_2} were calculated separately for daytime and nighttime CO_2 distributions and are reported here in terms of the average along both residual flow reaches. ± indicates 95% confidence intervals based on fitting uncertainties.

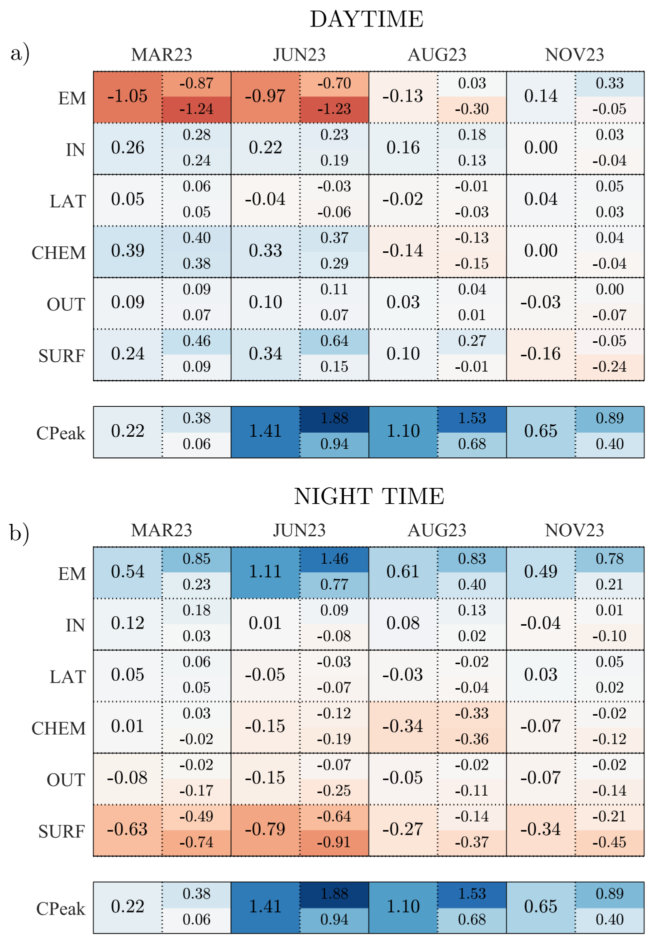

Figure 6. Quantification of the main CO_2 inputs and drivers (mol s^{-1}): metabolic input (EM); upstream input from the dams (IN); lateral inputs (LAT); carbonate buffering (CHEM); downstream transport (OUT); atmospheric exchange (SURF); carbopeaking (CPeak). (a): daytime; (b): nighttime. 95% confidence intervals are shown in the smaller sub-cells.

residual flow still acted as a sink for atmospheric CO_2 (SURF>0). In this case, CO_2 undersaturation was driven by carbonate buffering (CHEM), which was responsible for a "carbonate sink" of −0.14 mol s^{-1} (daytime) to −0.34 mol s^{-1} (night time). This contrasted with the positive CHEM input in Mar23 (0.39 μmol l^{-1}) and Jun23 (0.33 μmol l^{-1}) data set.

3.4. Measurements at the Hydropower Diversion Outlet

Figures 7 and 8 show the effects of hydropeaking on the flow rate, water temperature, and CO_2 fluxes, observed at site S16 for Jun23 and Nov23 data sets, respectively. The results for Mar23 and Aug23 data sets are shown in Figures S12 and S13 of the Supporting Information S1, respectively. Table 2 summarizes the variation in flow rate, water temperature, and CO_2 fluxes during hydropeaking compared to baseline conditions, for all data sets. Baseline conditions (i.e., without hydropeaking) were estimated based on the measurements at site S15 located upstream of the diversion outlet. The baseline k and F_{CO_2} values represent the gas transfer rate and intensity that would occur in the hydropeaking-affected reach in the absence of hydropeaking. They were calculated with the baseline Δ concentration measured at site S15 but based on the hydraulic conditions and channel geometry of site S16 with the baseline flow rate.

Sharp increases in flow rate Q (Figures 7a, 8a, S12a, and S13a in Supporting Information S1) at site S16 were indicative of hydropeaking activity, which caused the flow rate to increase by a factor of $Q_{peak}/Q_{baseline} \approx 5.5$ in as little as 20 min. Hydropeaking events occurred regularly during Jun23, Aug23, and Nov23 measurement campaigns, preferentially during the morning hours and in the late afternoon and through the evening. Mar23

10.1029/2024WR037834

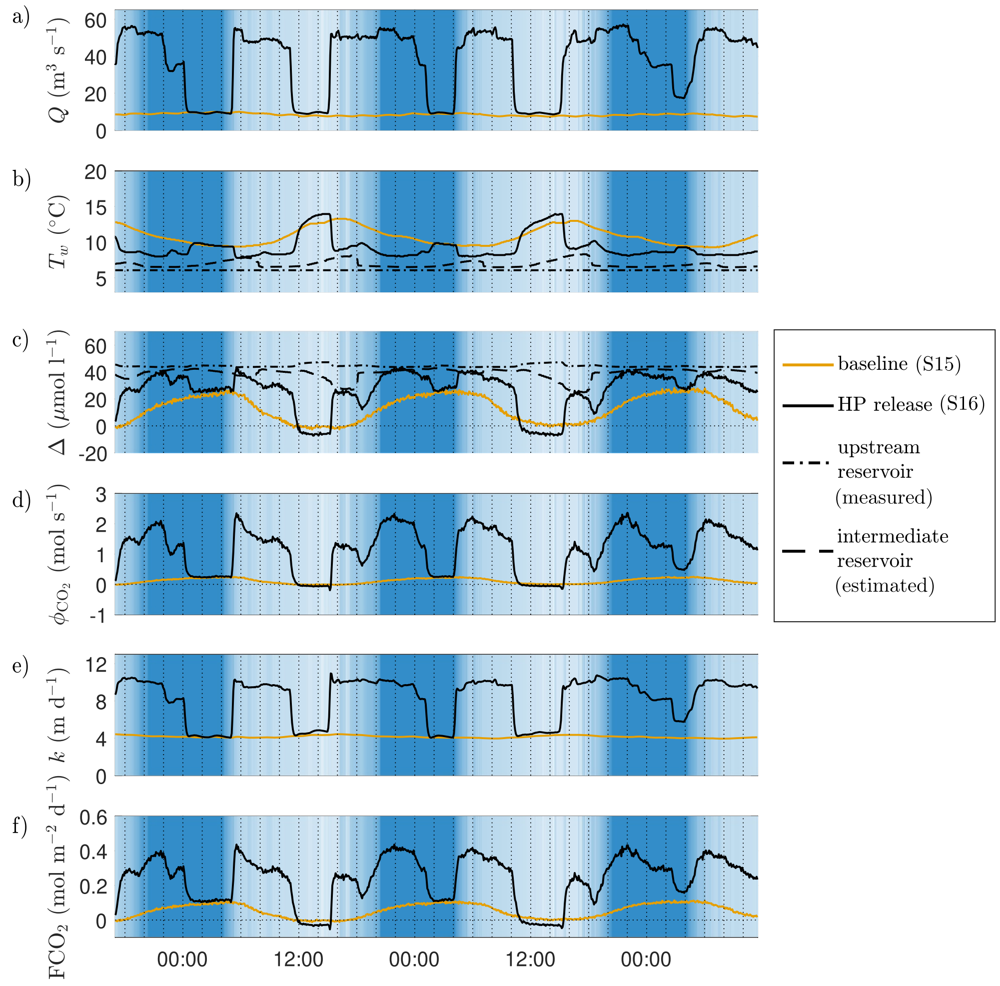

Figure 7. Time series of data measured during Jun23 campaign in the baseline flow (site S15–orange) and in the reach subject to hydropeaking (site S16–black). (a): estimated flow rate, Q; (b): measured water temperature, T_w; (c): measured excess CO_2 concentration, Δ; (d): calculated excess CO_2 mass flux, $\phi_{CO_2} = Q\Delta$; (e): estimated gas transfer rate, k; (f): estimated CO_2 evasion flux intensity, F_{CO_2} . Dashed-dotted line, black: measured conditions in the upstream reservoir, at the hydropower diversion intake. Dashed line, black: estimated conditions in the intermediate reservoir. Background colors represent the logarithm of the measured light intensity.

campaign saw only two sporadic, shorter (less than 2 hr long), and less intense ($Q_{\text{peak}}/Q_{\text{baseline}} \approx 4.5$) events. The moderate hydropower activity in Mar23 was likely in response to a scarcity of water in the upstream reservoir (see Figure 2) caused by a severe drought during the previous winter.

The measured water temperature patterns (Figures 7b, 8b, S12b, and S13b in Supporting Information S1) displayed a periodic diel fluctuation in the baseline flow which was more marked for Jun23 and Aug23 data sets, with higher T_w during the day. The release of colder water from the diversion outlet during Mar23, Jun23, and Aug23 campaigns caused a decrease in T_w during hydropeaking (cold thermopeaking, see Zolezzi et al., 2011), while warmer inflow from the hydropower system during Nov23 campaign caused warm thermopeaking (Figure 8b). Thermopeaking was caused by the contrast between the variation of the water temperature along the residual flow and the relatively constant temperature of the water that circulated within the hydropower diversion system, close to the water temperature at the intake level in the reservoir. The magnitude of thermopeaking was largest during the afternoon (up to 4.5 °C for Jun23 data set–Figure 7b), when the baseline value of T_w reached its maximum. The intermediate reservoir acted as a buffer for temperature fluxes, affecting the thermopeaking patterns. This became apparent after periods of inactivity in hydropower operation when the lack of input from the diversion

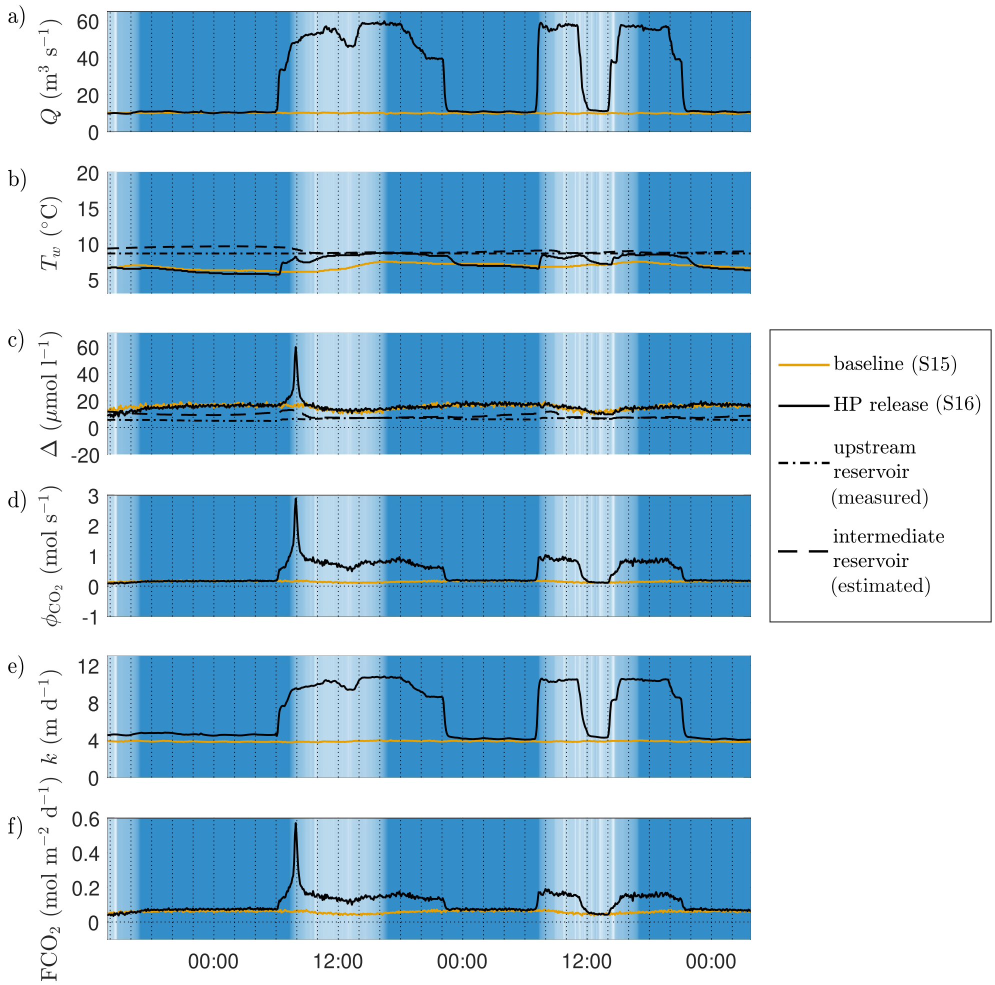

Figure 8. Time series of data measured during Nov23 campaign in the baseline flow (site S15–orange) and in the reach subject to hydropeaking (site S16–black). (a): estimated flow rate, Q; (b): measured water temperature, T_w; (c): measured excess CO_2 concentration, Δ; (d): calculated excess CO_2 mass flux, $\phi_{CO_2} = Q\Delta$; (e): estimated gas transfer rate, k; (f): estimated CO_2 evasion flux intensity, F_{CO_2} . Dashed-dotted line, black: measured conditions in the upstream reservoir, at the hydropower diversion intake. Dashed line, black: estimated conditions in the intermediate reservoir. Background colors represent the logarithm of the measured light intensity.

system, and the subsequent increase in residence time, caused the conditions within the intermediate reservoir to become more similar to those in the residual flow. For this reason, the measured time series of T_w for Jun23 data set had a small peak with a relative maximum at approximately 2.5 hr after the onset of hydropeaking. Our simple intermediate reservoir mixing model, represented by the dashed lines in Figure 7b, was able to predict the observed peak in the T_w time series at least qualitatively, confirming that the behavior was driven by mixing in the intermediate reservoir.

The time series of the excess CO_2 concentration Δ (Figures 7c, 8c, S12c, and S13c in Supporting Information S1) had a symmetric behavior compared to the water temperature dynamics, that is, higher CO_2 concentrations were observed during hydropeaking events or at night compared to the baseline. Diel $[CO_2]$ fluctuations driven by the ecosystem metabolism governed the baseline $[CO_2]$ dynamics like in the residual flow (Figure 3). These fluctuations remained identifiable at site S16 at times when the hydropower system was inactive. Hydropeaking events were strongly correlated with rapid increases in CO_2 concentrations and therefore in Δ for Mar23, Jun23 and Aug23 data sets (Figures 7c, S12c, and S13c in Supporting Information S1, respectively), while no clear variation in Δ during hydropeaking could be observed for Nov23 data set (Figure 8c). For Jun23 (Figure 7c) and Aug23 (Figure S13c in Supporting Information S1) data sets, the increase in Δ at the onset of hydropeaking was

Table 2
Measured CO_2 Parameters and Fluxes at the Hydropower Diversion Outlet During Baseline Flow and Hydropeaking

	Mar23		Jun23		Aug23		Nov23	
	Baseline	h-peak	Baseline	h-peak	Baseline	h-peak	Baseline	h-peak
Q ($m^3\ s^{-1}$)								
average	5.0	21.3	8.3	49.0	6.1	43.7	10.0	50.8
k ($m\ d^{-1}$)								
average	3.5	6.1	4.2	9.7	4.5	10.7	3.9	9.8
Λ (km)								
average	3.4	8.2	4.8	11.9	3.2	9.6	6.2	12.3
T_w (°C)								
night	6.6		9.4		14.1		6.1	
average	8.1	7.9	10.9	8.6	15.6	14.1	6.9	8.2
day	9.8		13.3		17.6		7.5	
Δ ($\mu mol\ l^{-1}$)								
night	27.3		27.0		31.4		19.1	
average	9.2	13.0	12.1	30.8	14.5	26.9	15.1	15.6
day	−12.5		−2.7		−4.8		9.5	
ϕ_{CO_2} ($mmol\ s^{-1}$)								
night	139.3		248.4		196.6		190.5	
average	47.1	270.8	106.1	1515.2	89.3	1184.5	151.1	789.1
day	−60.6		−21.6		−30.6		94.9	
F_{CO_2} ($\mu molm^{-2}\ s^{-1}$)								
night	1.11		1.27		1.60		0.85	
average	0.37	0.91	0.58	3.46	0.75	3.34	0.68	1.77
day	−0.53		−0.14		−0.26		0.43	

Note. The gas transfer rate k was evaluated according to Equation 3 and the turnover length scale Λ according to Equation 7.

typically followed by a temporary drop with a minimum after approximately 2.5 hr, and by a subsequent second and higher surge lasting until the end of the hydropeaking event. This behavior, which mirrored the T_w patterns, could be explained similarly by buffering within the intermediate reservoir.

$[CO_2]$ dynamics for Mar23 (Figure S12c in Supporting Information S1) and Nov23 (Figure 8c) data sets were more complex. In both cases, the predictions by our simple mixing model (represented by the dashed lines in Figures S12b and S12c in Supporting Information S1 and Figures 8b and 8c) did not match the observations of Δ and T_w, suggesting that the dynamics of mixing in the intermediate reservoir were not adequately captured. As an example, the Δ time-series measured during Nov23 campaign had an extremely sharp peak at around 8:00 of the first day, when Δ increased rapidly by around 40 $\mu mol\ l^{-1}$ in less than half an hour before going back to its initial value just as rapidly. Since this event occurred at the first occurrence of hydropeaking after multiple days of hydropower inactivity, the difference from the predicted behavior may have been caused by the asynchronous operation of the upstream and downstream power plants or by lateral influxes into the reservoir.

Excess CO_2 mass fluxes, $\phi_{CO_2} = Q\Delta$, were considerably higher during hydropeaking because of the combination of higher discharge and higher CO_2 concentration (Figures 7d, 8d, S12d, and S13d in Supporting Information S1). The increase in flow rate during hydropeaking was also associated with an increase in gas transfer rate k calculated according to Equation 3 (Figures 7e, 8e, S12e, and S13e in Supporting Information S1), and the combination of higher k and higher Δ yielded larger evasion fluxes F_{CO_2} (Figures 7f, 8f, S12f, and S13f in Supporting Information S1). Evasion fluxes at site S16, F_{CO_2}, were higher on average by a factor of 1.4 (Mar23) to 5.0 (Jun23) during hydropeaking. The various contributions to carbopeaking were quantified as described in

10.1029/2024WR037834

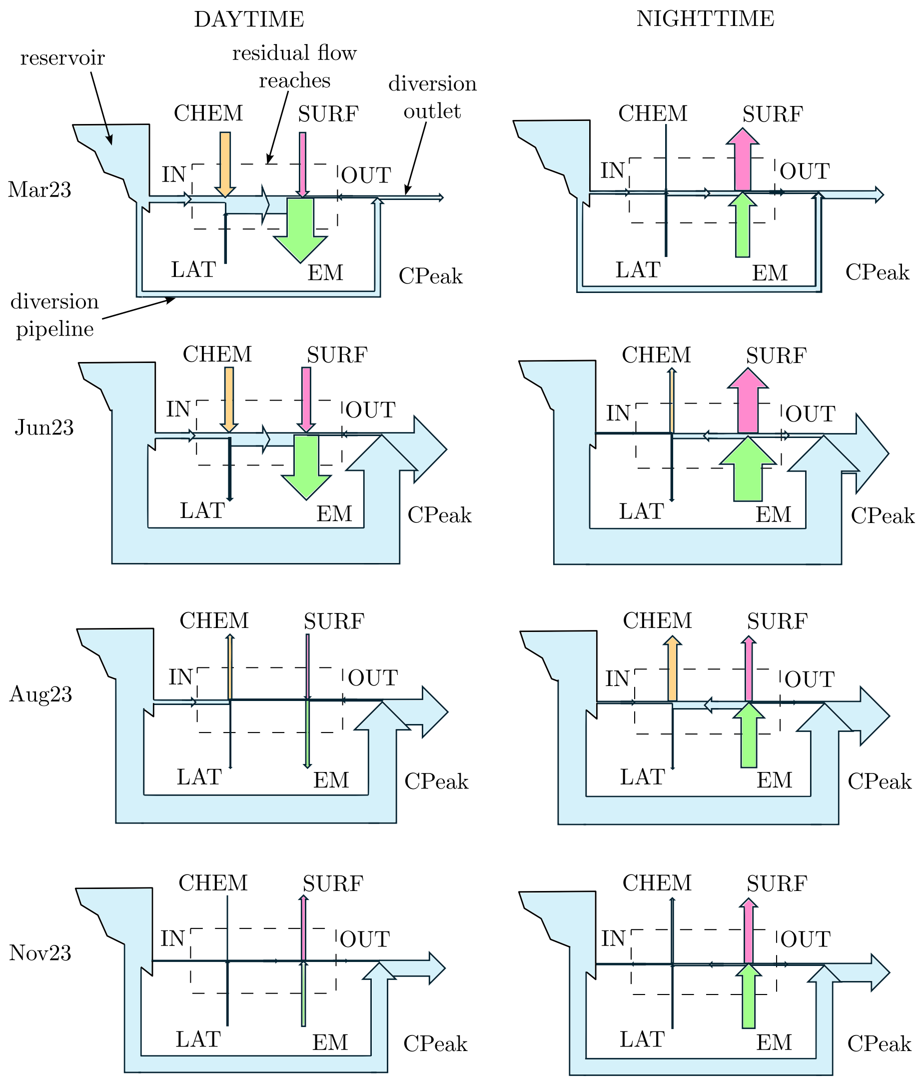

Figure 9. Schematic representation of the main CO_2 fluxes (arrows) contributing to CO_2 river balance. The arrow width is proportional to the magnitude of the fluxes. The upper pathway (dashed rectangle) represents the two residual flow reaches subject to multiple CO_2 fluxes: input from the dams (IN); carbonate buffering (CHEM); lateral input (LAT); atmospheric exchange (SURF); metabolic input (EM); downstream transport (OUT). The lower pathway represents the hydropower system (diversion pipeline and intermediate reservoir) insulated from external inputs, which releases a CO_2 flux (CPeak) at the hydropower outlet during hydropeaking. The upstream reservoir and the diversion pipeline outlet constitute the upstream and downstream boundaries of the system, respectively, where the two pathways merge. Changes in the magnitude and direction of the fluxes indicate different dominant CO_2 processes in different seasons and times of day. In the residual flow reaches, "vertical" (e.g., CHEM, LAT, SURF, and EM) fluxes are closely interconnected and predominant over "horizontal" (IN and OUT) fluxes, as expected given the relatively short turnover length scale Λ. CO_2 inputs from the reservoir bypass the residual flow effectively through the diversion pipeline but become largely predominant during hydropeaking in the hydropeaking-affected reach.

Section 2.6. Variations in Δ and k contributed similarly to F_{CO_2} except for Nov23 data set, when the increase in k was responsible for 98% of the average increase in F_{CO_2}. Transport fluxes ϕ_{CO_2} increased more strongly during hydropeaking than evasion fluxes, that is, by a factor of 4 (Nov23) to 13 (Jun23) on average. As a result, Λ (evaluated according to Equation 7) increased from between 3.2 and 6.2 km in baseline flow conditions, to between 8.2 and 12.3 km during hydropeaking. The increase in ϕ_{CO_2} was largely dominated by the flow rate, which contributed 76% (Jun23) to 99% (Nov23) of the variation.

3.5. CO_2 Input Due To Carbopeaking

The CO_2 input due to carbopeaking (indicated as CPeak in Figure 6) calculated according to Equation 23 varied from 0.22 mol s^{-1} (Mar23) to 1.41 mol s^{-1} (Jun23), and was close to the sum of all CO_2 fluxes (exchange and processing) along the two residual flow reaches. In fact, except for Mar23 when hydropeaking was limited, CPeak accounted for between 68% (night time, c.i. 43%–93%) and 144% (daytime, c.i. 90%–198%) of the L1 norm of all remaining terms of the CO_2 budget ($|EM| + |IN| + |LAT| + |CHEM| + |OUT| + |SURF|$). The magnitude of CPeak was particularly significant since carbopeaking was concentrated in time, during hydropeaking events, and in space, at the confluence of the diversion pipeline into the river, while the dominant CO_2 inputs (EM, CHEM, SURF) were the result of an integration along the two residual flow reaches.

4. Discussion

4.1. Drivers and Scales of CO_2 Fluxes in the Residual Flow Reaches

The quantification of the main CO_2 inputs across all data sets (Figures 6 and 9) demonstrates the variability of the contribution from different drivers across time scales. CO_2 fluxes along the residual flow reaches were dominated by metabolic inputs (EM), with a marked seasonal and diel dependence. Peak ecosystem activity was observed in Mar23 and Jun23 data sets, when the residual flow acted as a CO_2 sink during daytime. While the CO_2 input by respiration remained high throughout the year, we found that NEP was strongly reduced for Aug23 data set, and Nov23 data set, when the CO_2 daytime NEP sink disappeared leading to a positive net EM input.

For the Aug23 campaign, the decrease in productivity can be explained by a storm occurring 2–4 days before the measurements, causing substantial bed mobilization and a reduction in light penetration owing to increased water turbidity (Bernhardt et al., 2018; Peter et al., 2014). The concurrent increase in lateral CO_2 input for the Aug23 data set (indirectly, through carbonate buffering, CHEM) indicates a good lateral connectivity along the residual flow reaches. The significant "carbonate sink" (CHEM) observed for Aug23 data set was driven by a lateral inflow with high TA (4.82 ± 0.58 mmol l^{-1}), high pH (9.0 ± 0.1), but low CO_2 concentration ($\Delta_L = -7.8$ μmol l^{-1}), which mixed with the less alkaline water of the stream driving a shift of the carbonate equilibrium and hence a decrease in un-ionized $[CO_2]$. Indeed, the strong contribution of CHEM coincided with a higher longitudinal gradient in TA and DIC along the residual flow (relative increase of 56% between the upstream dam and the diversion pipeline outlet, compared to an average of 25% for the other data sets), which was likely connected to the same storm event that affected NEP.

The Mar23 data set had a relatively large (0.39 μmol l^{-1}) positive CHEM input which could not be explained by lateral inflow, since the Mar23 campaign followed a period of sustained lack of precipitation when the estimated increase in flow rate and TA due to lateral inputs were at a minimum (30% and 23% along the whole residual flow length, respectively). For this data set (and similarly but with lesser magnitude for Jun23 data set), the CHEM input was sustained by the in-stream re-equilibration of the carbonate system, which counteracted the rapid decrease in daytime $[CO_2]$ driven by atmospheric evasion within a few kilometres downstream of the dam. Under conditions of relatively low $[CO_2]$ and high alkalinity, carbonate buffering can account for up to 90% of emissions (Winnick & Saccardi, 2024).

The consumption or production of CO_2 by the ecosystem metabolism and, to a lesser extent, by carbonate buffering were mostly compensated by the exchange with the atmosphere (SURF). The relatively large contribution of evasion fluxes despite the small magnitude of Δ along most of the residual flow was justified by the high gas transfer rate and consistent with the relatively short Λ compared to the reach length. Indeed, the overall length of the residual flow was approximately $7 \times \Lambda$, meaning that the whole CO_2 stock was renewed around 7 times through mostly metabolic activity and surface exchange. The magnitude of CO_2 inputs from the dams (IN) changed according to the $[CO_2]$ distribution inside the upstream reservoir, with the largest values in Mar23 and smaller values in Nov23. Downstream export fluxes, OUT, reflected the shift in Δ driven by the ecosystem metabolism, therefore, they always acted toward counteracting the effects of EM.

4.2. Scaling and Generality

Hydropower regulation can impact CO_2 fluxes by introducing additional inputs of CO_2 in the tailwaters of the dam or during hydropeaking, and by altering the spatiotemporal scales of the fluxes. In the residual flow, the input of CO_2 from the dams was significant but limited to a short distance of approximately 2.5 km. Beyond this distance, the main drivers of CO_2 fluxes were those typical of non-regulated mountain streams, that is, lateral inputs, ecosystem metabolism, and carbonate buffering (Boix Canadell et al., 2021; Horgby, Boix Canadell et al., 2019; Horgby, Segatto, et al., 2019; Saccardi & Winnick, 2021). We quantified peak primary productivity (GPP_{peak}) and respiration rates (ER) between 1.23 and 7.30 μmol m^{-2} s^{-1} and between 1.73 and 3.91 μmol m^{-2} s^{-1}, respectively. Our estimates of ER were slightly higher than global average expectations for temperate streams (1.56 μmol m^{-2} s^{-1}: Battin et al. (2023)) and than measurements in prealpine stream networks (Roberts et al., 2007; Saccardi & Winnick, 2021), but they were within the range of other Alpine streams (0–19.6 μmol m^{-2} s^{-1}: (Ulseth et al., 2018)) and close to observations in regulated reaches in the Pyrenees (Aristi et al., 2014) (see Table 1 of the Supporting Information S1 for a more detailed comparison between GPP, ER, and NEP estimates in our work and previous studies).

Expectations for the evasion flux intensity vary greatly in the literature because of the strong heterogeneity of the drivers of CO_2 concentration and gas transfer rate. Our estimates of average F_{CO_2} in the residual flow reaches (-2.2 to 1.1 μmol m^{-2} s^{-1} at daytime and 2.0 to 5.4 μmol m^{-2} s^{-1} at nighttime) were generally within the expected range for mountain rivers (see Table S2 of the Supporting Information S1). Global average expectations vary between 3.57 μmol m^{-2} s^{-1} (2.75–4.49) for streams and small rivers in the temperate zone (Lauerwald et al., 2015) and 2.9 μmol m^{-2} s^{-1} (-1.43 to 137.4) in global mountain rivers (Horgby, Segatto, et al., 2019). Higher evasion rates (18.0–43.1 μmol m^{-2} s^{-1}, see Horgby, Boix Canadell et al. (2019)) were measured in Swiss Alpine streams with significantly steeper slopes than in our study case.

CO_2 concentrations in the upstream reservoir were one order of magnitude smaller than previously observed in tropical and subtropical reservoirs (Calamita et al., 2021; Guérin et al., 2006; Kemenes et al., 2016; Wu et al., 2024), but comparable to the concentrations observed in other Alpine reservoirs (Diem et al., 2012; Pighini et al., 2018). Compared to a previous study by Calamita et al. (2021) focused on CO_2 fluxes and dynamics downstream of a tropical reservoir (Lake Kariba), the drivers and the scales of CO_2 fluxes in our study case were markedly different, as they were directly influenced by the design of the hydropower system and by the different spatiotemporal scales and drivers of mountain rivers. Downstream of the Kariba Dam there were no residual flow reaches. The river slope was much smaller (0.01%–0.03%), and the discharge was much larger (~1500 m^3 s^{-1}), therefore transport was expected to dominate over surface exchange. The variation in CO_2 concentration downstream of the dam was by large the dominant component ($\sim 80\%$) of carbopeaking (Calamita et al., 2021). Such a variation was caused by the selective activation of multiple turbine intakes located above and below a strong vertical $[CO_2]$ gradient inside the reservoir.

In our study case, carbopeaking was governed by the increase in flow rate (76%–99%) rather than concentration. Although the intakes that supplied the residual flow and the hydropower system were located at different depths like in the Kariba reservoir, this difference had a marginal effect on carbopeaking. Instead, the discontinuity in CO_2 concentration during hydropeaking was caused primarily by the decoupling of CO_2 fluxes along the residual flow and the hydropower diversion pathways. This was the result of (a) the spatial separation between the dam and the hydropower release outlet and (b) the disparity of temporal scales (e.g., transit time) between the residual flow and the diversion system: the spatial separation drove a substantial drift of the CO_2 concentration along the long (relative to Λ) residual flow, leading to a very different concentration directly upstream of the hydropower diversion outlet; the scale disparity allowed minimal CO_2 leakage and equilibration within the hydropower system (including the intermediate reservoir) so that the outflow from the diversion pipeline was still considerably supersaturated in CO_2. Our data revealed the importance of these two contributions to the occurrence of carbopeaking: for Nov23 data set, the little metabolic activity in the residual flow and the low supersaturation inside the reservoir limited the streamwise gradient in CO_2 concentration along the residual flow making the spatial separation ineffective; for Mar23 data set, the magnitude of carbopeaking was inhibited by prolonged inactivity of the hydropower system which drove an increase in transit time in the diversion pipeline. In both cases, CPeak was smaller than in Jun23 and Aug23. Since the mode of operation and geometry of the hydropower system in our study site is fairly common at least across the Alpine area, we expect these controls of carbopeaking to have widespread relevance in this context.

5. Conclusions

Hydropower regulation can significantly alter the spatiotemporal distribution of carbon and CO_2 fluxes by introducing shorter sub-daily variations and highly localized inputs and by breaking the space-time continuity of the river network. These alterations add to the natural heterogeneity and complexity of CO_2 drivers across river systems, especially in Alpine rivers, posing additional challenges for the quantification and understanding of CO_2 fluxes. We combined spatially and temporally resolved field data with numerical modeling to quantify the main drivers of CO_2 fluxes along an Alpine river regulated by a cascading hydropower diversion system, which includes two reaches subject to residual flow (minimum flow) regulation, and a reach subject to hydropeaking. To our knowledge, this was the first application of an inverse CO_2 modeling approach that included carbonate buffering, demonstrating the importance of its contribution to the CO_2 budget. CO_2 drivers and dynamics in the residual flow were similar to those observed in non-regulated rivers, except in the first $\sim$2.5 km downstream of the dams where the reservoir released a substantial additional CO_2 input. In contrast, carbopeaking had a strong impact on the magnitude and dynamics of CO_2 fluxes within the hydropeaking-impacted reach. We quantified an effect of carbopeaking comparable to the cumulative magnitude of all CO_2 fluxes integrated along both residual flow reaches at peak daytime and/or nighttime.

One of the main scientific challenges to enable the quantification and understanding of the role of rivers in global carbon cycling is to determine to what degree direct (e.g., damming) and indirect (e.g., climate change) anthropogenic perturbation affects riverine carbon fluxes (Dean & Battin, 2024). Our work contributed to this objective by shedding new light on the fundamental processes governing CO_2 fluxes in a regulated river within the Alpine context, where the separation between natural and anthropogenic drivers is subtle, and where climate change is rapidly transforming the hydrology and biogeochemistry of catchments. The capability of our combined measurement/modeling approach to simultaneously quantify multiple drivers of CO_2 fluxes is key to monitoring the response of the ecosystem metabolism to hydrological alterations, complementing the traditional assessment of the ecological status of rivers. Integrating this approach into large-scale and long-term carbon observation systems (Dean & Battin, 2024) will help clarify and predict the response of fluvial ecosystems and rivers biogeochemistry to climate change and anthropogenic pressures on a regional and global scale.

Data Availability Statement

All data sets for this research are openly available at the following URL: https://doi.org/10.5281/zenodo.11032052 (Dolcetti, 2024).

Acknowledgments
This work was supported by Fondazione Caritro through a Bando Post-Doc Grant (2021.0225, *Quantificazione delle emissioni di gas serra in corsi d'acqua alpini soggetti a hydropeaking*). We acknowledge support by the Italian Ministry of Universities and Research (MUR) in the framework of the project DICAM-EXC (Departments of Excellence 2023–2027, Grant L232/2016). Financed by the European Union–Next Generation EU, Mission 4 Component 2 –CUP 20222W5WXC. The Authors are grateful to the Associate Editor, to E. Bertuzzo, and to two anonymous Reviewers for their helpful comments. The Authors are grateful to H.A. Dijkstra and to Utrecht University for loaning the MicroCTD, to L. Forti, F. Sartori, A. Bampi, and P. Scarfiello for their assistance with the preparation of the experimental setup, to M. De Vincenzi and G. Donini for their help during the field campaigns, to A. Marzadri for helpful disscussions, and to W. Vaona and R. Di Maggio for the assistance with laboratory analysis. Open access publishing facilitated by Universita degli Studi di Trento, as part of the Wiley - CRUI-CARE agreement.

References

Aristi, I., Arroita, M., Larrañaga, A., Ponsatí, L., Sabater, S., von Schiller, D., et al. (2014). Flow regulation by dams affects ecosystem metabolism in Mediterranean rivers. *Freshwater Biology*, *59*(9), 1816–1829. https://doi.org/10.1111/fwb.12385

Battin, T. J., Lauerwald, R., Bernhardt, E. S., Bertuzzo, E., Gener, L. G., Hall Jr, R. O., et al. (2023). River ecosystem metabolism and carbon biogeochemistry in a changing world. *Nature*, *613*(7944), 449–459. https://doi.org/10.1038/s41586-022-05500-8

Bencala, K. E., & Walters, R. A. (1983). Simulation of solute transport in a mountain pool-and-riffle stream: A transient storage model. *Water Resources Research*, *19*(3), 718–724. https://doi.org/10.1029/wr019i003p00718

Bernhardt, E. S., Heffernan, J. B., Grimm, N. B., Stanley, E. H., Harvey, J., Arroita, M., et al. (2018). The metabolic regimes of flowing waters. *Limnology & Oceanography*, *63*(S1), S99–S118. https://doi.org/10.1002/lno.10726

Beven, K., & Westerberg, I. (2011). On red herrings and real herrings: Disinformation and information in hydrological inference. *Hydrological Processes*, *25*(10), 1676–1680. https://doi.org/10.1002/hyp.7963

Boix Canadell, M., Escoffier, N., Ulseth, A. J., Lane, S. N., & Battin, T. J. (2019). Alpine glacier shrinkage drives shift in dissolved organic carbon export from quasi-chemostasis to transport limitation. *Geophysical Research Letters*, *46*(15), 8872–8881. https://doi.org/10.1029/2019gl083424

Boix Canadell, M., Gómez-Gener, L., Ulseth, A. J., Clémençon, M., Lane, S. N., & Battin, T. J. (2021). Regimes of primary production and their drivers in Alpine streams. *Freshwater Biology*, *66*(8), 1449–1463. https://doi.org/10.1111/fwb.13730

Brighenti, S., Tolotti, M., Bruno, M. C., Wharton, G., Pusch, M. T., & Bertoldi, W. (2019). Ecosystem shifts in Alpine streams under glacier retreat and rock glacier thaw: A review. *Science of the Total Environment*, *675*, 542–559. https://doi.org/10.1016/j.scitotenv.2019.04.221

Bruno, M. C., Maiolini, B., Carolli, M., & Silveri, L. (2009). Impact of hydropeaking on hyporheic invertebrates in an Alpine stream (Trentino, Italy). *Annales de limnologie-international journal of limnology*, *45*(3), 157–170. https://doi.org/10.1051/limn/2009018

Bruno, M. C., Maiolini, B., Carolli, M., & Silveri, L. (2010). Short time-scale impacts of hydropeaking on benthic invertebrates in an Alpine stream (Trentino, Italy). *Limnologica*, *40*(4), 281–290. https://doi.org/10.1016/j.limno.2009.11.012

Bruno, M. C., Vallefuoco, F., Casari, A., Larsen, S., Dallafior, V., & Zolezzi, G. (2023). Moving waters to mitigate hydropeaking: A case study from the Italian Alps. *River Research and Applications*, *39*(3), 570–587. https://doi.org/10.1002/rra.4086

Calamita, E., Siviglia, A., Gettel, G. M., Franca, M. J., Winton, R. S., Teodoru, C. R., et al. (2021). Unaccounted CO_2 leaks downstream of a large tropical hydroelectric reservoir. *Proceedings of the National Academy of Sciences*, *118*(25), e2026004118. https://doi.org/10.1073/pnas.2026004118

Ciais, P., Dolman, A. J., Bombelli, A., Duren, R., Peregon, A., Rayner, P. J., et al. (2014). Current systematic carbon-cycle observations and the need for implementing a policy-relevant carbon observing system. *Biogeosciences*, *11*(13), 3547–3602. https://doi.org/10.5194/bg-11-3547-2014

Comiti, F. (2012). How natural are Alpine mountain rivers? Evidence from the Italian Alps. *Earth Surface Processes and Landforms*, *37*(7), 693–707. https://doi.org/10.1002/esp.2267

Conroy, H. D., Hotchkiss, E. R., Cawley, K. M., Goodman, K., Hall Jr, R. O., Jones, J. B., et al. (2023). Seasonality drives carbon emissions along a stream network. *Journal of Geophysical Research: Biogeosciences*, *128*(8), e2023JG007439. https://doi.org/10.1029/2023jg007439

Dean, J. F., & Battin, T. J. (2024). Future directions for river carbon biogeochemistry observations. *Nature Water*, *2*(3), 1–4. https://doi.org/10.1038/s44221-024-00207-8

DEE. (2022). Dolomiti Edison Energy S.r.L., Dichiarazione ambientale impianti idroelettrici dell'asta Noce e impianto di Pozzolago, triennio 2021-23. Retrieved from https://www.dee.tn.it/wr-resource/ent3/1/Dichiarazione-Ambientale-Convalidata-21-23.pdf

Deemer, B. R., Yackulic, C. B., Hall Jr, R. O., Dodrill, M. J., Kennedy, T. A., Muehlbauer, J. D., et al. (2022). Experimental reductions in subdaily flow fluctuations increased gross primary productivity for 425 river kilometers downstream. *PNAS nexus*, *1*(3), pgac094. https://doi.org/10.1093/pnasnexus/pgac094

Demars, B. O. L., Thompson, J., & Manson, J. R. (2015). Stream metabolism and the open diel oxygen method: Principles, practice, and perspectives. *Limnology and Oceanography: Methods*, *13*(7), 356–374. https://doi.org/10.1002/lom3.10030

Dickson, A. G., Sabine, C. L., & Christian, J. R., (Eds.). (2007). *Guide to best practices for ocean CO_2 measurements* (PICES Special Publication, 3; IOCCP Report 8: p. 191). North Pacific Marine Science Organization. https://doi.org/10.25607/OBP-1342

Diem, T., Koch, S., Schwarzenbach, S., Wehrli, B., & Schubert, C. J. (2012). Greenhouse gas emissions (CO_2–CH_4–N_2O) from several perialpine and alpine hydropower reservoirs by diffusion and loss in turbines. *Aquatic Sciences*, *74*(3), 619–635. https://doi.org/10.1007/s00027-012-0256-5

Dolcetti, G. (2024). CO_2 fluxes measurement data set for the lower segment of the River Noce, Italy [Dataset]. https://doi.org/10.5281/zenodo.11032052

Duvert, C., Butman, D. E., Marx, A., Ribolzi, O., & Hutley, L. B. (2018). CO_2 evasion along streams driven by groundwater inputs and geomorphic controls. *Nature Geoscience*, *11*(11), 813–818. https://doi.org/10.1038/s41561-018-0245-y

Galy-Lacaux, C., Delmas, R., Jambert, C., Dumestre, J.-F., Labroue, L., Richard, S., & Gosse, P. (1997). Gaseous emissions and oxygen consumption in hydroelectric dams: A case study in French Guyana. *Global Biogeochemical Cycles*, *11*(4), 471–483. https://doi.org/10.1029/97gb01625

Gomez-Gener, L., Rocher-Ros, G., Battin, T., Cohen, M. J., Dalmagro, H. J., Dinsmore, K. J., et al. (2021). Global carbon dioxide efflux from rivers enhanced by high nocturnal emissions. *Nature Geoscience*, *14*(5), 289–294. https://doi.org/10.1038/s41561-021-00722-3

Guérin, F., Abril, G., Richard, S., Burban, B., Reynouard, C., Seyler, P., & Delmas, R. (2006). Methane and carbon dioxide emissions from tropical reservoirs: Significance of downstream rivers. *Geophysical Research Letters*, *33*(21). https://doi.org/10.1029/2006gl027929

Hall, R. O., Jr., & Ulseth, A. J. (2020). Gas exchange in streams and rivers. *Wiley Interdisciplinary Reviews: Water*, *7*(1), e1391. https://doi.org/10.1002/wat2.1391

Hall, R. O., Jr., Yackulic, C. B., Kennedy, T. A., Yard, M. D., Rosi-Marshall, E. J., Voichick, N., & Behn, K. E. (2015). Turbidity, light, temperature, and hydropeaking control primary productivity in the Colorado river, Grand Canyon. *Limnology & Oceanography*, *60*(2), 512–526. https://doi.org/10.1002/lno.10031

Harmon, T. C. (2020). Carbon gas flux to and from inland waters: Support for a global observation network. *Limnology*, *21*(3), 429–442. https://doi.org/10.1007/s10201-020-00623-1

Hauer, C., Siviglia, A., & Zolezzi, G. (2017). Hydropeaking in regulated rivers: From process understanding to design of mitigation measures. *Science of the Total Environment*, *579*, 22–26. https://doi.org/10.1016/j.scitotenv.2016.11.028

Hayes, D. S., Bruno, M. C., Alp, M., Boavida, I., Batalla, R. J., Bejarano, M. D., et al. (2023). 100 key questions to guide hydropeaking research and policy. *Renewable and Sustainable Energy Reviews*, *187*, 113729. https://doi.org/10.1016/j.rser.2023.113729

Hayes, D. S., Schülting, L., Carolli, M., Greimel, F., Batalla, R. J., & Casas-Mulet, R. (2022). Hydropeaking: Processes, effects, and mitigation. *Encyclopedia of Inland Waters*, 134–149. https://doi.org/10.1016/b978-0-12-819166-8.00171-7

Hertwich, E. G. (2013). Addressing biogenic greenhouse gas emissions from hydropower in LCA. *Environmental Science & Technology*, *47*(17), 9604–9611. https://doi.org/10.1021/es401820p

Hood, E., Battin, T. J., Fellman, J., O'neel, S., & Spencer, R. G. (2015). Storage and release of organic carbon from glaciers and ice sheets. *Nature Geoscience*, *8*(2), 91–96. https://doi.org/10.1038/ngeo2331

Horgby, Å., Boix Canadell, M., Ulseth, A. J., Vennemann, T. W., & Battin, T. J. (2019). High-resolution spatial sampling identifies groundwater as driver of CO_2 dynamics in an Alpine stream network. *Journal of Geophysical Research: Biogeosciences*, *124*(7), 1961–1976. https://doi.org/10.1029/2019jg005047

Horgby, Å., Segatto, P. L., Bertuzzo, E., Lauerwald, R., Lehner, B., Ulseth, A. J., et al. (2019). Unexpected large evasion fluxes of carbon dioxide from turbulent streams draining the world's mountains. *Nature Communications*, *10*(1), 4888. https://doi.org/10.1038/s41467-019-12905-z

Hotchkiss, E. R., Hall Jr, R. O., Sponseller, R. A., Butman, D., Klaminder, J., Laudon, H., et al. (2015). Sources of and processes controlling CO_2 emissions change with the size of streams and rivers. *Nature Geoscience*, *8*(9), 696–699. https://doi.org/10.1038/ngeo2507

Kanduč, T., Mori, N., Kocman, D., Stibilj, V., & Grassa, F. (2012). Hydrogeochemistry of Alpine springs from north Slovenia: Insights from stable isotopes. *Chemical Geology*, *300*, 40–54. https://doi.org/10.1016/j.chemgeo.2012.01.012

Kemenes, A., Forsberg, B. R., & Melack, J. M. (2016). Downstream emissions of CH_4 and CO_2 from hydroelectric reservoirs (Tucuruí, Samuel, and Curuá-Una) in the Amazon basin. *Inland Waters*, *6*(3), 295–302. https://doi.org/10.1080/iw-6.3.980

Koschorreck, M., Prairie, Y. T., Kim, J., & Marcé, R. (2020). CO_2 is not like CH_4 – Limits of and corrections to the headspace method to analyse pCO_2 in water. *Biogeosciences*, *2020*, 1–12. https://doi.org/10.5194/bg-18-1619-2021

Lauerwald, R., Laruelle, G. G., Hartmann, J., Ciais, P., & Regnier, P. A. (2015). Spatial patterns in CO_2 evasion from the global river network. *Global Biogeochemical Cycles*, *29*(5), 534–554. https://doi.org/10.1002/2014gb004941

Lennox, R. J., Thiemer, K., Vollset, K. W., Pulg, U., Stranzl, S., Nilsen, C. I., et al. (2022). Behavioural response of brown trout (Salmo trutta) to total dissolved gas supersaturation in a regulated river. *Ecohydrology*, *15*(1), e2363. https://doi.org/10.1002/eco.2363

Maavara, T., Chen, Q., Van Meter, K., Brown, L. E., Zhang, J., Ni, J., & Zarfl, C. (2020). River dam impacts on biogeochemical cycling. *Nature Reviews Earth & Environment*, *1*(2), 103–116. https://doi.org/10.1038/s43017-019-0019-0

MeteoTrentino stazioni meteorologiche. (2023). T0408 Mezzolombardo (Maso delle Part). Retrieved from http://storico.meteotrentino.it/web.htm?ppbm=T0408&rs&1&df

MeteoTrentino stazioni meteorologiche. (2003). T0397 Cles (Maso Maiano). Retrieved from http://storico.meteotrentino.it/web.htm?ppbm=T0397&rs&1&df

Moog, D. B., & Jirka, G. H. (1999). Stream reaeration in nonuniform flow: Macroroughness enhancement. *Journal of Hydraulic Engineering*, *125*(1), 11–16. https://doi.org/10.1061/(asce)0733-9429(1999)125:1(11)

Moreira, M., Hayes, D. S., Boavida, I., Schletterer, M., Schmutz, S., & Pinheiro, A. (2019). Ecologically-based criteria for hydropeaking mitigation: A review. *Science of the Total Environment*, *657*, 1508–1522. https://doi.org/10.1016/j.scitotenv.2018.12.107

Odum, H. T. (1956). Primary production in flowing waters. *Limnology & Oceanography*, *1*(2), 102–117. https://doi.org/10.4319/lo.1956.1.2.0102

Parasiewicz, P. (2007). The MesoHABSIM model revisited. *River Research and Applications*, *23*(8), 893–903. https://doi.org/10.1002/rra.1045

PAT. (2012). Provincia Autonoma di Trento, Dipartimento Urbanistica ed Ambiente, Servizio Utilizzazione Acque Pubbliche. Bilanci Idrici, Relazione Tecnica - Il Bacino del Noce. Retrieved from http://osservatorio.energia.provincia.tn.it/bilanci_idrici/aspetti%20quantit%C3%A0%20APRIE/03_Relazione_tecnica_noce.pdf

PAT. (2023). Provincia Autonoma di Trento, Dipartimento Protezione Civile, Ufficio Dighe. *Mezzolombardo Ponte Rupe - idrometro fiume Noce*. Retrieved from https://www.floods.it/public/Charts.php?Sensori[]=11691

Pennington, R., Argerich, A., & Haggerty, R. (2018). Measurement of gas-exchange rate in streams by the oxygen–carbon method. *Freshwater Science*, *37*(2), 222–237. https://doi.org/10.1086/698018

Peter, H., Singer, G. A., Preiler, C., Chifflard, P., Steniczka, G., & Battin, T. J. (2014). Scales and drivers of temporal pCO_2 dynamics in an Alpine stream. *Journal of Geophysical Research: Biogeosciences*, *119*(6), 1078–1091. https://doi.org/10.1002/2013jg002552

Pighini, S., Ventura, M., Miglietta, F., & Wohlfahrt, G. (2018). Dissolved greenhouse gas concentrations in 40 lakes in the Alpine area. *Aquatic Sciences*, *80*(3), 1–13. https://doi.org/10.1007/s00027-018-0583-2

Pulg, U., Vollset, K. W., Velle, G., & Stranzl, S. (2016). First observations of saturopeaking: Characteristics and implications. *Science of the Total Environment*, *573*, 1615–1621. https://doi.org/10.1016/j.scitotenv.2016.09.143

Roberts, B. J., Mulholland, P. J., & Hill, W. R. (2007). Multiple scales of temporal variability in ecosystem metabolism rates: Results from 2 years of continuous monitoring in a forested headwater stream. *Ecosystems*, *10*(4), 588–606. https://doi.org/10.1007/s10021-007-9059-2

Rocher-Ros, G., Sponseller, R. A., Lidberg, W., Mörth, C.-M., & Giesler, R. (2019). Landscape process domains drive patterns of CO_2 evasion from river networks. *Limnology and Oceanography Letters*, *4*(4), 87–95. https://doi.org/10.1002/lol2.10108

Saccardi, B., & Winnick, M. (2021). Improving predictions of stream CO_2 concentrations and fluxes using a stream network model: A case study in the East river watershed, CO, USA. *Global Biogeochemical Cycles*, *35*(12), e2021GB006972. https://doi.org/10.1029/2021gb006972

Schelker, J., Singer, G. A., Ulseth, A. J., Hengsberger, S., & Battin, T. J. (2016). CO_2 evasion from a steep, high gradient stream network: Importance of seasonal and diurnal variation in aquatic pCO_2 and gas transfer. *Limnology & Oceanography*, *61*(5), 1826–1838. https://doi.org/10.1002/lno.10339

Segatto, P. L., Battin, T. J., & Bertuzzo, E. (2023). A network-scale modeling framework for stream metabolism, ecosystem efficiency, and their response to climate change. *Water Resources Research*, *59*(3), e2022WR034062. https://doi.org/10.1029/2022wr034062

Shi, W., Maavara, T., Chen, Q., Zhang, J., Ni, J., & Tonina, D. (2023). Spatial patterns of diffusive greenhouse gas emissions from cascade hydropower reservoirs. *Journal of Hydrology*, *619*, 129343. https://doi.org/10.1016/j.jhydrol.2023.129343

Silverthorn, T., López-Rojo, N., Foulquier, A., Chanudet, V., & Datry, T. (2023). Greenhouse gas dynamics in river networks fragmented by drying and damming. *Freshwater Biology*, *68*(12), 2027–2041. https://doi.org/10.1111/fwb.14172

Soued, C., & Prairie, Y. T. (2020). The carbon footprint of a Malaysian tropical reservoir: Measured versus modelled estimates highlight the underestimated key role of downstream processes. *Biogeosciences*, *17*(2), 515–527. https://doi.org/10.5194/bg-17-515-2020

Stets, E. G., Butman, D., McDonald, C. P., Stackpoole, S. M., DeGrandpre, M. D., & Striegl, R. G. (2017). Carbonate buffering and metabolic controls on carbon dioxide in rivers. *Global Biogeochemical Cycles*, *31*(4), 663–677. https://doi.org/10.1002/2016gb005578

Toffolon, M., Siviglia, A., & Zolezzi, G. (2010). Thermal wave dynamics in rivers affected by hydropeaking. *Water Resources Research*, *46*(8). https://doi.org/10.1029/2009wr008234

Ulseth, A. J., Bertuzzo, E., Singer, G. A., Schelker, J., & Battin, T. J. (2018). Climate-induced changes in spring snowmelt impact ecosystem metabolism and carbon fluxes in an Alpine stream network. *Ecosystems*, *21*(2), 373–390. https://doi.org/10.1007/s10021-017-0155-7

Ulseth, A. J., Hall, R. O., Jr., Boix Canadell, M., Madinger, H. L., Niayifar, A., & Battin, T. J. (2019). Distinct air–water gas exchange regimes in low-and high-energy streams. *Nature Geoscience*, *12*(4), 259–263. https://doi.org/10.1038/s41561-019-0324-8

Wanninkhof, R. (1992). Relationship between wind speed and gas exchange over the ocean. *Journal of Geophysical Research*, *97*(C5), 7373–7382. https://doi.org/10.1029/92JC00188

Winnick, M. J., & Saccardi, B. (2024). Impacts of carbonate buffering on atmospheric equilibration of CO_2, $\delta^{13}C_{DIC}$, and $\delta^{14}C_{DIC}$ in rivers and streams. *Global Biogeochemical Cycles*, *38*(2), e2023GB007860. https://doi.org/10.1029/2023gb007860

Winton, R. S., Calamita, E., & Wehrli, B. (2019). Reviews and syntheses: Dams, water quality and tropical reservoir stratification. *Biogeosciences*, *16*(8), 1657–1671. https://doi.org/10.5194/bg-16-1657-2019

Wu, Z., Yu, D., Yu, Q., Liu, Q., Zhang, M., Dahlgren, R. A., et al. (2024). Greenhouse gas emissions (CO_2–CH_4–N_2O) along a large reservoir-downstream river continuum: The role of seasonal hypoxia. *Limnology & Oceanography*, *69*(5), 1015–1029. https://doi.org/10.1002/lno.12544

Zarfl, C., Lumsdon, A. E., Berlekamp, J., Tydecks, L., & Tockner, K. (2015). A global boom in hydropower dam construction. *Aquatic Sciences*, *77*(1), 161–170. https://doi.org/10.1007/s00027-014-0377-0

Zolezzi, G., Siviglia, A., Toffolon, M., & Maiolini, B. (2011). Thermopeaking in alpine streams: Event characterization and time scales. *Ecohydrology*, *4*(4), 564–576. https://doi.org/10.1002/eco.132

References From the Supporting Information

Appling, A. P., Hall, R. O. Jr., Yackulic, C. B., & Arroita, M. (2018). Overcoming equifinality: Leveraging long time series for stream metabolism estimation. *Journal of Geophysical Research: Biogeosciences*, *123*(2), 624–645. https://doi.org/10.1002/2017jg004140

Bastviken, D., Nygren, J., Schenk, J., Parellada Massana, R., & Duc, N. T. (2020). Facilitating the use of low-cost methane (CH_4) sensors in flux chambers–calibration, data processing, and an open-source make-it-yourself logger. *Biogeosciences*, *17*(13), 3659–3667. https://doi.org/10.5194/bg-17-3659-2020

Bastviken, D., Sundgren, I., Natchimuthu, S., Reyier, H., & G˚alfalk, M. (2015). Cost-efficient approaches to measure carbon dioxide (CO_2) fluxes and concentrations in terrestrial and aquatic environments using mini loggers. *Biogeosciences*, *12*(12), 3849–3859. https://doi.org/10.5194/bg-12-3849-2015

Brinkerhoff, C. B., Gleason, C. J., Zappa, C. J., Raymond, P. A., & Harlan, M. E. (2022). Remotely sensing river greenhouse gas exchange velocity using the SWOT satellite. *Global Biogeochemical Cycles*, *36*(10), e2022GB007419. https://doi.org/10.1029/2022gb007419

Clow, D. W., Striegl, R. G., & Dornblaser, M. (2021). Spatiotemporal dynamics of CO_2 gas exchange from headwater mountain streams. *Journal of Geophysical Research: Biogeosciences*, *126*(9), e2021JG006509. https://doi.org/10.1029/2021jg006509

Crawford, J. T., Dornblaser, M. M., Stanley, E. H., Clow, D. W., & Striegl, R. G. (2015). Source limitation of carbon gas emissions in high-elevation mountain streams and lakes. *Journal of Geophysical Research: Biogeosciences*, *120*(5), 952–964. https://doi.org/10.1002/2014jg002861

Hauet, A., Morlot, T., & Daubagnan, L. (2018). Velocity profile and depth-averaged to surface velocity in natural streams: A review over a large sample of rivers. *E3s web of conferences* (Vol. 40, p. 06015). EDP Sciences. https://doi.org/10.1051/e3sconf/20184006015

Johnson, M. S., Billett, M. F., Dinsmore, K. J., Wallin, M., Dyson, K. E., & Jassal, R. S. (2010). Direct and continuous measurement of dissolved carbon dioxide in freshwater aquatic systems—method and applications. *Ecohydrology: Ecosystems, Land and Water Process Interactions, Ecohydrogeomorphology*, *3*(1), 68–78. https://doi.org/10.1002/eco.95

Lewis, E., Wallace, D., & Allison, L. J. (1998). Program developed for CO_2 system calculations (p. 2). US Department of Energy Technical Report. https://doi.org/10.2172/639712

Nocedal, J., Öztoprak, F., & Waltz, R. A. (2014). An interior point method for nonlinear programming with infeasibility detection capabilities. *Optimization Methods and Software*, *29*(4), 837–854. https://doi.org/10.1080/10556788.2013.858156

Sharp, J. D., Pierrot, D., Humphreys, M. P., Epitalon, J.-M., Orr, J. C., Lewis, E. R., & Wallace, D. W. (2020). CO2SYS v3 for MATLAB. *Zenodo*. https://doi.org/10.5281/zenodo.3950563

Vingiani, F., Durighetto, N., Klaus, M., Schelker, J., Labasque, T., & Botter, G. (2021). Evaluating stream CO_2 outgassing via drifting and anchored flux chambers in a controlled flume experiment. *Biogeosciences*, *18*(3), 1223–1240. https://doi.org/10.5194/bg-18-1223-2021

Welber, M., Le Coz, J., Laronne, J. B., Zolezzi, G., Zamler, D., Dramais, G., et al. (2016). Field assessment of noncontact stream gauging using portable surface velocity radars (SVR). *Water Resources Research*, *52*(2), 1108–1126. https://doi.org/10.1002/2015wr017906